geotechnics

MDPI

Review

A One-Dimensional Model Used for the Analysis of Seismic Site Response and Soil Instabilities: A Review of SCOSSA 1.0 Computer Code

Giuseppe Tropeano [1] and Anna Chiaradonna [2,*]

[1] Department of Civil, Environmental Engineering and Architecture, University of Cagliari, Via Marengo 2, 09123 Cagliari, Italy; giuseppe.tropeano@unica.it
[2] Department of Civil, Construction-Architectural and Environmental Engineering, University of L'Aquila, 67100 L'Aquila, Italy
* Correspondence: anna.chiaradonna1@univaq.it; Tel.: +39-08624507

Abstract

This review aims to provide a complete and comprehensive state of the art of the SCOSSA computer code, which is a one-dimensional nonlinear computer code used for the analysis of seismic site response and soil instability. Indeed, among the effects of earthquakes, the activation of landslides and liquefaction constitute two of the predominant causes of vulnerability in the physical and built environment. The SCOSSA computer code (Seismic Code for Stick–Slip Analysis) was initially developed to evaluate the permanent displacements of simplified slopes using a coupled model, and introduced several improvements with respect to the past, namely, the formulation for solving the dynamic equilibrium equations incorporates the capability for automated detection of the critical sliding surface; an up-to-date constitutive model to represent hysteretic material behavior and a stable iterative algorithm to support the solution of the system in terms of kinematic variables. To address liquefaction-induced failure, a simplified pore water pressure generation model was subsequently developed and integrated into the code, coupled with one-dimensional consolidation theory. This review retraces the main features, developments, and applications of the computer code from the origin to the present version.

Keywords: seismic response analysis; liquefaction; pore pressure; modified hyperbolic model; extended Masing rules; cyclic response model; earthquake; nonlinear dynamic analysis; Port Island seismic array; centrifuge tests

Academic Editor: Salvatore Grasso

Received: 28 September 2025
Revised: 8 December 2025
Accepted: 22 December 2025
Published: 25 December 2025

1. Introduction

Italian building code (D.M. 17.01.2018) [1], as well as several national codes, prescribe seismic response analyses for specific site conditions. These analyses, typically using 1D codes, model the vertical propagation of shear waves through a soil column. The approach is either linear or equivalent nonlinear, though these methods are unable to directly assess seismic site instability. In practice, even in high-risk areas, simplified procedures are used instead.

While research has developed rigorous, highly sophisticated soil constitutive models to address these issues, their use in practical design is limited due to the complexity of calibrating numerous parameters. Methods balancing scientific rigor with practical application were developed for specific earthwork types (e.g., [2]), but a lack of general solutions persists. This may stem from a historical view that soil failure under dynamic

conditions is a rare event, only occurring during high-intensity earthquakes. However, recent earthquakes (e.g., 2009 L'Aquila, 2012 Emilia, 2016 Central Italy) have challenged this belief, as more timely and accurate damage reconnaissance has allowed engineers and researchers to recognize the manifestations of site instability.

Seismic site instability is essentially due to an increase in shear stresses as a result of wave propagation in deformable soils (collapse and landslides), or decreased effective stresses caused by increasing pore water pressures (subsidence, liquefaction, and landslides), resulting in a drastic decrease in soil stiffness and shear strength.

Rigorous numerical modeling of seismic instability requires sophisticated computer codes with advanced constitutive models that incorporate plasticity and volumetric–distortional coupling. These models can simulate localized or generalized failure, but their practical use is challenging due to the difficulty of calibrating numerous parameters reliably.

A compromise between scientific rigor and practical application is achieved through simplified models. Many of these methods are decoupled, meaning they separate the seismic wave propagation problem (solved under free-field conditions) from the estimation of response parameters (e.g., displacement or cyclic stress ratio) using empirical or semi-empirical procedures. While useful for initial screening, these decoupled methods may not adequately capture the highly nonlinear behavior of soils nearing failure.

For failure problems, several "coupled" stick–slip formulations have been proposed to calculate plastic displacements. SCOSSA (Seismic Code for Stick–Slip Analysis) was developed by Tropeano et al. [3]. It includes an algorithm to automatically detect critical sliding surfaces, an updated hysteretic constitutive relationship, and a stable iterative solution for kinematic variables.

Regarding liquefaction problems, several studies pointed out the importance of performing effective stress analysis [4–6], especially for studying layered soil deposits [7–9] and sand ejecta problems [6,10,11]. As a consequence, several constitutive models [12–19] or cyclic response models associated with pore pressure generation models [20,21] were developed.

SCOSSA-PWP [22] incorporates a simplified stress-based pore water pressure model [23] along with one-dimensional consolidation theory [24]. This model was chosen for its simplicity, consistency with established liquefaction frameworks, ease of implementation, and straightforward parameter quantification. Originally calibrated using laboratory tests, the model was later extended to use common in situ test data (CPT and SPT) [25], and, more recently, DMT [26].

The code's effectiveness in predicting pore water pressure build-up and dissipation has been validated against physical models in seismic centrifuges [22,27,28] and instrumented field sites [22,25,27]. Comparisons with more complex codes on real and ideal cases [29,30] show that SCOSSA provides a slightly more conservative, yet reliable, prediction. Post-analysis results have also been successfully used to predict horizontal displacements [31] and post-consolidation settlements [27] in real-world case studies, yielding estimates consistent with observed damage.

This review traces the main steps of the code's development, main features, and applications by summarizing the work performed on the code in the last ten years.

2. Main Steps in the Development of the SCOSSA Code

The code was originally developed to evaluate permanent seismic displacements of slopes [32], considering a stick–slip model (see Figure 1). In detail, a lumped-mass formulation was adopted with more generalized assumptions, and the model was implemented in the first version of the computer code, named "ACST", which used an equivalent-linear

formulation expressed in the time domain. In Tropeano et al.'s research [33], the version in non-linear conditions is presented for the first time.

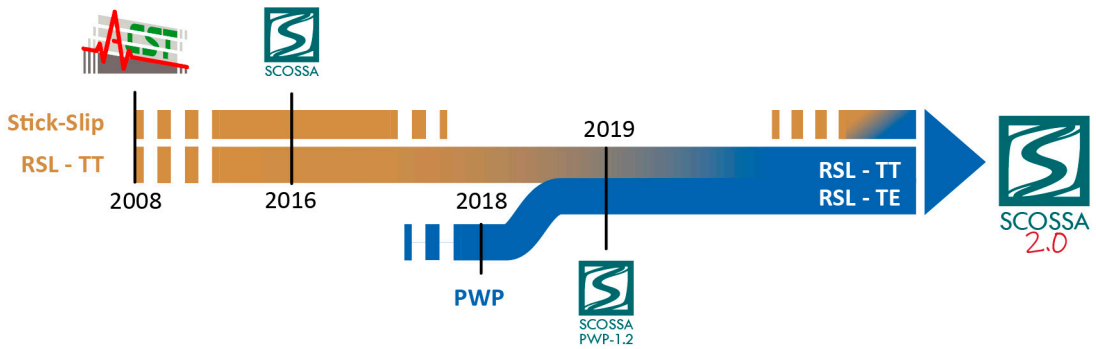

Figure 1. SCOSSA development timeline.

Tropeano et al. [3] describes a new version, renamed "SCOSSA" (Seismic Code for Stick–Slip Analysis), where (1) the solution of the dynamic equilibrium equations includes the possibility of searching for the critical sliding surface automatically, (2) the constitutive relationship models hysteretic soil behavior, and (3) a stable iterative algorithm solves the system in terms of kinematic variables.

So, initially, the code was designed for dynamic analyses of total stress to simulate both the transient response (stick mode) and response in the case of the formation of a rupture and a sliding surface (stick–slip mode). Two distinct analysis modes were implemented in the code: the 'RSL-TT' module, which solves the equations of motion to provide the site's seismic response under total stress conditions; and the 'Stick-Slip' module, which includes the possibility of a sliding mechanism in the local seismic response. The "RSL-TT" module performs nonlinear analysis of a soil column composed of horizontal layers under total stress conditions. The "Stick-Slip" module is used to determine the depth of the sliding surface of an indefinite slope and therefore, calculate the sliding response and cumulative displacements.

The "RSL-TT" module for transient seismic response has been verified and validated with other codes during the Prediction of Non-linear Soil Behaviour (PreNoLin) project, an international numerical benchmark [34,35].

The use of "Stick-Slip" modules has been limited to theoretical exercises and a few well-documented case histories of slope instability [3]. Further applications include the modeling of the combined response of soil and building, based on the case study of a structure damaged after the 2009 L'Aquila earthquake [36].

In the framework of the Chiaradonna PhD thesis, a pore water pressure model following a simplified stress-based approach has been developed [23] and implemented in the "RSL-TT" module of the code [22,37]. The pore pressure model was implemented using a loosely coupled approach to account for the degradation of soil stiffness and strength. This degradation is a result of the progressive build-up of pore water pressure caused by cyclic shear loading. The new version of the code, hereafter called "SCOSSA PWP", consists of the modified "RSL-TT" module integrated with the above-mentioned pore pressure model and 1D consolidation theory [24]. The dissipation and redistribution of excess pore water pressure can be activated or deactivated in the analysis settings by enabling the execution of effective stress analysis, both in totally undrained and partially drained conditions, respectively.

In the following three main chapters, the calculations performed for solving seismic response analysis in total stress ('RSL-TT' module), slope stability ('Stick-Slip' module), and liquefaction problems ('SCOSSA PWP'), are detailed, as well as the available validations.

3. Seismic Response Analysis in Total Stress

The soil profile is modeled in the code as a system of consistent lumped masses connected by viscous dampers and hysteretic nonlinear springs (Figure 2a,b).

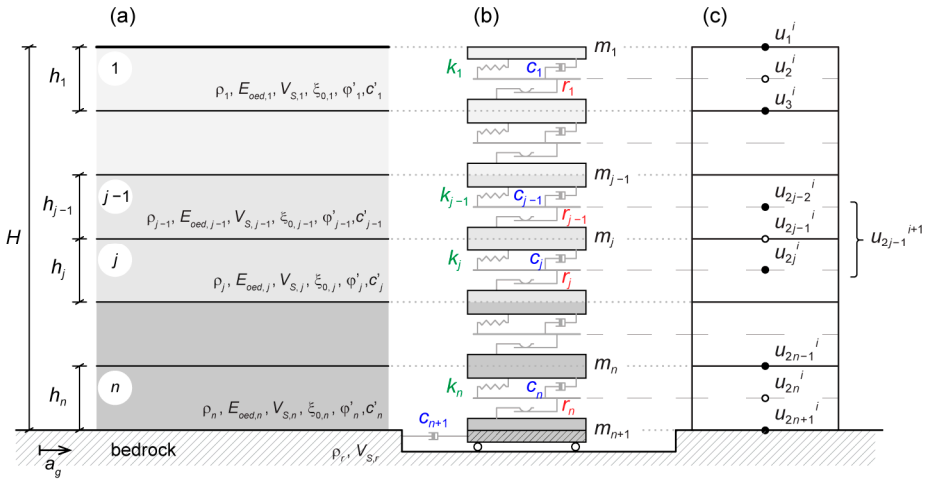

Figure 2. Soil column modeling: (**a**) layered soil parameters; (**b**) lumped mass and (**c**) dissipation model discretirzation [22].

The discretization of the subsurface profile into a lumped parameter system has been automatically implemented within the code. This implementation is based on the Kuhlemeyer and Lysmer [38] criterion, which mandates that the maximum sub-layer thickness be constrained to a specific fraction (typically 1/6 to 1/8) of the minimum wavelength, which must be accurately transmitted. This maximum thickness is, however, still subjected to a lower bound constraint, which corresponds to the minimum significant thickness (approximately 25 cm).

The code conducts nonlinear seismic response analyses by solving the dynamic equilibrium of a Multiple-Degree-Of-Freedom (MDOF) system in the time domain. The seismic response quantified by absolute displacements, s, resulting from a base ground motion, a_g (Figure 2a,b), is determined through the integration of the system:

$$\mathbf{M}\,\ddot{\mathbf{s}} + \mathbf{C}\,\dot{\mathbf{s}} + \mathbf{K}\,\mathbf{s} = \mathbf{f}(t) \tag{1}$$

where $\mathbf{f}(t)$ is the vector of applied forces, and $\mathbf{M}$, $\mathbf{C}$, and $\mathbf{K}$ are the mass, damping, and stiffness matrices, respectively. The $\mathbf{f}$ vector can be set equal to

$$\mathbf{f}(t) = \mathbf{i} \cdot \begin{cases} c_n v_g(t) + k_n s_g(t) & \text{(inside motion with rigid bedrock)} \\ 2\,c_n v_g(t) & \text{(inside motion with deformable bedrock)} \\ c_{n+1} v_g(t) & \text{(outcrop motion with deformable bedrock)} \end{cases} \tag{2}$$

where the following apply:

- $\mathbf{i}$ is a vector with each element equal to zero, except for the n-th (for inside motion), or $(n + 1)$th (for outcrop motion), equal to unity;
- $v_g(t)$ and $s_g(t)$ are, respectively, the velocity and the displacement time histories obtained by numerical integration of input acceleration, $a_g(t)$;
- c_n and k_n are, respectively, the viscous damping coefficient and the spring elastic stiffness for the n-th element;
- $c_{n+1} = \rho_r V_{S,r}$ is the bedrock seismic impedance.

The matrices **M** and **K** are defined, respectively, from the mass, m_j, and the current spring stiffness, k_j, of a generic soil layer j, as

$$m_1 = \frac{\rho_1 h_1}{2};\ m_j = \frac{\rho_j h_j + \rho_{j-1} h_{j-1}}{2};\ m_{n+1} = \frac{\rho_n h_n}{2} \tag{3}$$

$$k_j = \frac{G_j}{h_j} \tag{4}$$

where, for the j-th layer, ρ_j, h_j, and G_j are, respectively, the density, thickness, and tangent shear modulus.The viscous damping matrix, **C**, is defined following the full Rayleigh damping formulation [39]:

$$\mathbf{C} = \alpha_R \mathbf{M} + \beta_R \mathbf{K} \tag{5}$$

where α_R and β_R are constants defined as a function of the minimum soil damping ratio, ξ_{min}, the fundamental frequency of the soil column and the predominant frequency of the input motion (according to a double frequency control approach) [40]. The two frequencies are internally computed during the setting phase of the analysis, and no input data are requested from the user, unlike other codes (see following Section 3.2.1).

The vector of input forces, $\mathbf{f}(t)$, is initially updated for the i-th time step.

The code numerically integrates the equations by using the Newmark β method [41]:

$$\begin{cases} \mathbf{M}\,\ddot{\mathbf{s}}_{i+1} + \mathbf{C}\,\dot{\mathbf{s}}_{i+1} + \mathbf{K}\,\mathbf{s}_{i+1} = \mathbf{f}_{i+1} \\ \dot{\mathbf{s}}_{i+1} = \dot{\mathbf{s}}_i + \Delta t\ (1-\gamma_N)\ \ddot{\mathbf{s}}_i + \Delta t\,\gamma_N\,\ddot{\mathbf{s}}_{i+1} \\ \mathbf{s}_{i+1} = \mathbf{s}_i + \Delta t\,\dot{\mathbf{s}}_i + \Delta t^2\,(1/2-\beta_N)\,\ddot{\mathbf{s}}_i + \Delta t^2 \beta_N\,\ddot{\mathbf{s}}_{i+1} \end{cases} \tag{6}$$

$\gamma_N = 0.5$ and $\beta_N = 0.25$ are the default coefficients, so that the method is unconditionally stable and no numerical damping is introduced.

For a dynamic system with n degrees of freedom, the system (6) can be easily solved if expressed in the following form:

$$\mathbf{A}\mathbf{x}_{t+1} = \mathbf{B}\mathbf{x}_t + \mathbf{q}_{t+1} \tag{7}$$

where **x** is the vector of the unknown variables:

$$\mathbf{x} = \left\{ \ddot{\mathbf{s}}^T \quad \dot{\mathbf{s}}^T \quad \mathbf{s}^T \right\}^T \tag{8}$$

In Equation (7), **q** is the external forces vector, where the first n elements are equal to **f**, as defined in Equation (2), and the remaining $2n$ elements are null; **A** and **B** are the matrices of the integration method, defined as follows:

$$\mathbf{A} = \begin{bmatrix} \mathbf{M} & \mathbf{C} & \mathbf{K} \\ -\Delta t\ \gamma_N\ \mathbf{I} & \mathbf{I} & \mathbf{0} \\ -\Delta t^2\ \beta_N\ \mathbf{I} & \mathbf{0} & \mathbf{I} \end{bmatrix};\ \mathbf{B} = \begin{bmatrix} \mathbf{0} & \mathbf{0} & \mathbf{0} \\ \Delta t(1-\gamma_N)\ \mathbf{I} & \mathbf{I} & \mathbf{0} \\ \Delta t(1/2-\beta_N)\mathbf{I} & \Delta t\ \mathbf{I} & \mathbf{I} \end{bmatrix} \tag{9}$$

where **1** and **0** are the unit and null matrix, respectively, with $n \times n$ dimensions.

The numerical solution of system (7) is carried out adopting an exact inversion method based on the Crout-Doolittle factorization algorithm, modified for band matrices. The kinematic variables, i.e., acceleration, velocity and displacement, are computed from the numerical solution. Then, the shear strain increment, $\Delta\gamma j$, is computed as:

$$\Delta\gamma_j = \frac{\Delta s_j - \Delta s_{j+1}}{h_j} \tag{10}$$

where $\Delta s_j = (s_j)_{i+1} - (s_j)_i$ is the variation of the displacement in the time interval Δt, while h_j is the sub-layer thickness.

Given that the matrix of the stiffness, **K**, exhibits strain-dependent variability, the initial computational effort involves assuming the stiffness matrix to be equivalent to the value calculated during the preceding time increment.

A continuous stress-strain function is employed to calculate the shear stress increment, $\Delta\tau_j$, in the time interval Δt. This calculation is executed as a function of the shear strain level mobilized at the prior time step (via the cyclic response model detailed in Section 3.1).

For the j-th sub-layer, the current value of stiffness, k_j, is calculated by the tangent shear modulus, G_j, as

$$k_j = \frac{G_j(\gamma_j)}{h_j} \tag{11}$$

As a consequence, the stiffness matrix is defined from the current shear strain level through Equation (11).

An iterative calculation *ir* required at each time step due to the mutual dependency between **K** and the solution of the system. As a first attempt, the stiffness matrix is set equal to the one calculated at the previous time instant, i.e., $[\mathbf{K}^{t+1}]_{k=0} = \mathbf{K}^t$. The strain, $[\gamma^{t+1}]_{k=0}$, and stress, $[\tau^{t+1}]_{k=0}$, vectors are calculated from the solution of the system. Then, the stiffness matrix of the layering is again evaluated as $[\mathbf{K}^{t+1}]_{k=1}$. The processe is iterated until the maximum value of the relative error, ε_{rel}, of two subsequent solutions, $[\mathbf{x}^{t+1}]_{k-1}$ and $[\mathbf{x}^{t+1}]_k$, is less than a fixed tolerance value, ε_{toll}. The maximum value of the relative error, ε_{rel} is defined as:

$$\varepsilon_{rel} = \max\left\{ \frac{\left| [x_j]_k^{t+1} - [x_j]_{k-1}^{t+1} \right|}{10^{-6} + \left| [x_j]_k^{t+1} \right|} \right\} \text{ with } j = 1,\ 2,\ \ldots,\ n \text{ (layer index)} \tag{12}$$

3.1. Cyclic Response Model

The nonlinear hysteretic behavior of the soil is simulated utilizing an extended formulation of the Modified Kondner–Zelasko (MKZ) hyperbolic model (e.g., [42]). The MKZ model was selected among several hyperbolic models because it reproduces soil behavior over quite large strain levels with a limited number of required parameters, clearly defined in laboratory tests. Indeed, the model is implemented in several computer codes (DEEPSOIL [43], OpenSees [44], etc.) because it is numerically stable by reducing numerical noise and improves convergence in time-integration schemes. In addition, this model can be easily modified to include enhancements.

The MKZ model is delineated by two distinct constitutive relationships: one for the initial loading phase and the other governing unloading–reloading cycles.

The stress–strain constitutive function (i.e., the backbone curve) for the loading condition is expressed as follows:

$$\tau(\gamma) = \frac{\gamma G_0}{1 + \beta(\gamma/\gamma_r)^s} \tag{13}$$

where β and s are two dimensionless factors, γ is the shear strain level, G_0 is the initial shear modulus, and γ_r is the reference shear strain.

The stress–strain relationship for the unloading–reloading condition can be either defined by the generalized Masing criteria or by considering damping control given by the unload–reload curves proposed by Phillips and Hashash [45]:

$$\tau = F(\gamma_m) \cdot \left[\frac{G_0(\gamma - \gamma_c)}{1 + \beta\left(\frac{\gamma - \gamma_c}{2\gamma_r}\right)^s} - \frac{G_0(\gamma - \gamma_c)}{1 + \beta\left(\frac{\gamma_m}{2\gamma_r}\right)^s} \right] + \frac{G_0(\gamma - \gamma_c)}{1 + \beta\left(\frac{\gamma_m}{2\gamma_r}\right)^s} + \tau_c \tag{14}$$

In Equation (14), γ_c and τ_c are the reversal shear strain and shear stress, respectively, γ_m is the maximum shear strain reached during the time history, and $F(\gamma_m)$ is a damping reduction factor, defined as

$$F(\gamma_m) \doteq \frac{\xi_{\exp}(\gamma)}{\xi_{Mas}(\gamma)} = p_1 - p_2\left(1 - \frac{G(\gamma_m)}{G_0}\right)^{p_3} \quad (15)$$

In Equation (15), p_1, p_2, and p_3 are dimensionless coefficients derived from the optimal fitting of the ratio between the strain-dependent hysteretic damping as measured in laboratory tests, $\xi_{exp}(\gamma)$, and the correspondent one estimated via the Masing rules, $\xi_{Mas}(\gamma)$; $G(\gamma_m)$ represents the secant shear modulus corresponding to the maximum shear strain γ_m (see [45] for details).

The revised formulation adjusts the Masing unloading–reloading criteria, thereby achieving enhanced correlation with the experimental damping–strain curves, particularly at elevated shear strain levels. In terms of numerical execution, the application of the factor $F(\gamma_m)$ concurrently induces a marked progressive reduction in the small-strain shear stiffness, G_0, thus simulating a cyclic soil degradation.

Within the SCOSSA framework, the three parameters defining the modified MKZ model (Equation (13)) and the parameters governing the modified Masing rules (Equation (14)) are archived in a database that incorporates established literature curves [45]. These relationships are presented to the user during the subsoil data input process via an interface dialog box. As an alternative, these parameters can be defined specifically for a project through nonlinear multi-regression analysis of the experimental data points for $G(\gamma)/G_0$ and $\xi(\gamma)$, and subsequently appended to the database. A dedicated utility was integrated into SCOSSA for the interpolation of objective functions. This procedure is executed by an adaptive algorithm that computes the relative minimum value of the multivariate functions, which was enhanced with an optimization protocol to determine the bracketing interval.

Table 1 summarizes the parameters of the cyclic response model and the procedure used for their definition based on the results of soil investigations.

Table 1. Definition of the parameters for the cyclic response model.

Parameter	Source	Calibration
Low-strain shear modulus (G_0)	Shear wave velocity measurements	Internally computed during the analysis as product of soil density ρ and shera wave velocity V_S, i.e., $G_0 = \rho\ {V_S}^2$
MKZ parameters (β, s and γ_r)	G/G_0 vs. shear strain curve from laboratory tests (e.g., resonant column; cyclic torsional shear; strain-based cyclic triaxial)	Nonlinear multi-regression analysis of the experimental data points integrated in a dedicated utility of SCOSSA
Damping ratio (ξ_{exp} vs. γ)	Damping ratio vs. shear strain curve from laboratory tests (e.g., resonant column; cyclic torsional shear; strain-based cyclic triaxial)	Not needed
Damping ratio control coefficients (p_1, p_2, and p_3)	Damping ratio vs. shear strain curve from laboratory tests compared with analytical Masing formaultation.	Nonlinear multi-regression analysis of the experimental data points inte-grated in a dedicated utility of SCOSSA

3.2. Code Performances at Low–Medium Strains

Soil nonlinearity is a function of the shear strain level mobilized during seismic shaking [46,47]. The following two subsections illustrate the code's performance at both low and medium–high strain levels. The first concerns simulating the behavior of ideal soil columns, and the second concerns a real case study investigated within the framework of the PreNoLin project [35].

3.2.1. Verification on Ideal Soil Profiles

The first ideal model consists of a 20 m column of homogeneous soil with linear visco-elastic behavior (Figure 3a). To test the performance of the code in the visco-elastic linear range of the soil, the visco-elastic linear analysis carried out with SCOSSA was compared with those of eight computer codes listed in Table 2 [48]. The first five codes perform the analysis in a 1D condition, while the remaining are among the most popular codes for 2D and 3D seismic response analysis used in professional practice.

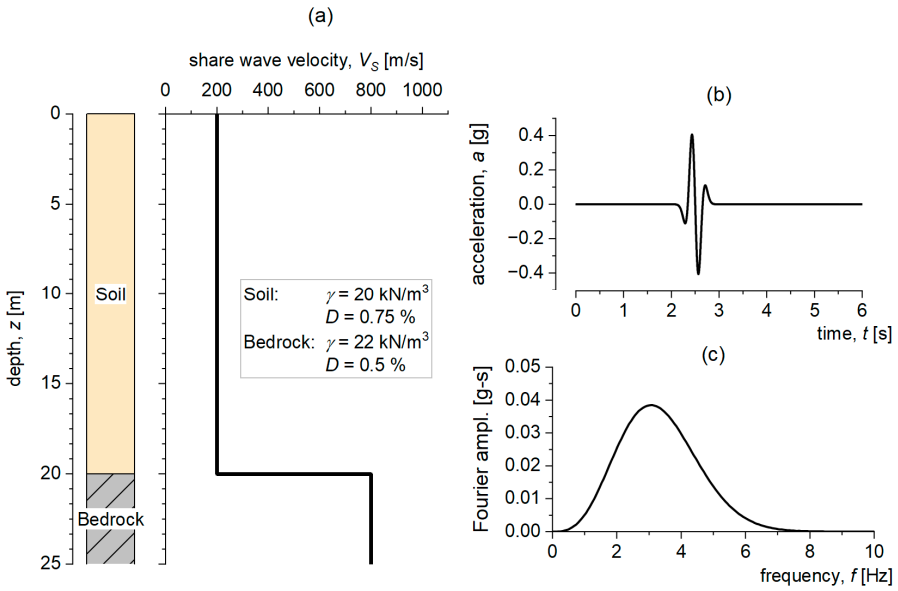

Figure 3. Ideal soil column: stratigraphy and the corresponding shear wave velocity profile (**a**); reference seismic motion recorded on rock outcrop, presented as the acceleration time history (where the achieved Peak Ground Acceleration (PGA) is denoted by a symbol) (**b**) and the associated Fourier amplitude spectrum (**c**) [48].

Table 2. Capability and main features of the computer codes used in the comparison [48].

Computer Code	Reference	Geometry	Frequency Control Approach for Rayleigh Damping	Rayleigh Damping Parameters Requested as Input Data	Total Stress		Effective Stress		Computational Effort
					Equivalent Linear	Non-Linear	Loosely Coupled	Fully Coupled	
EERA	[49]	1D	-	-	✓				Low
STRATA	[50]		-	-	✓				Low
DEEPSOIL	[43]		double/fourth	no	✓	✓	✓		Low
SCOSSA	[22]		double	no		✓	✓		Low
Cyclic1D	[51]		double	yes				✓	Low
Quake/W	[52]	2D	double	yes	✓	✓	✓		High
PLAXIS	[53]		double	yes		✓		✓	High
FLAC	[54]		single	yes		✓	✓	✓	High
FLAC3D	[55]	3D	single	yes		✓	✓	✓	Very High

The soil is defined by a unit weight of 20 kN/m^3 and a shear wave velocity, V_S, of 200 m/s, which remains invariant with depth. The dissipative behavior of the soil is defined by damping ratio, D, equal to 0.75%. This deformable layer rests upon a rock half-space

that serves as the seismic bedrock. The bedrock exhibits a unit weight of 22 kN/m^3, a shear wave velocity, V_S, of 800 m/s and a damping ratio of 0.5%.

The soil column is excited by an impulsive loading, similar to a Ricker-β wavelet type waveform, recorded on a hypothetical rigid outcrop rock (outcrop motion). This motion reaches a Peak Ground Acceleration (PGA), of 0.4 g centered on a frequency of about 3 Hz (Figure 3b,c), which is close to the natural frequency of the soil column, i.e., 2.5 Hz.

Details on the models as defined in the different adopted codes can be found in [48].

The results are expressed in terms of the time history of acceleration at ground level (Figure 4). The time histories of the acceleration at the surface overlap perfectly.

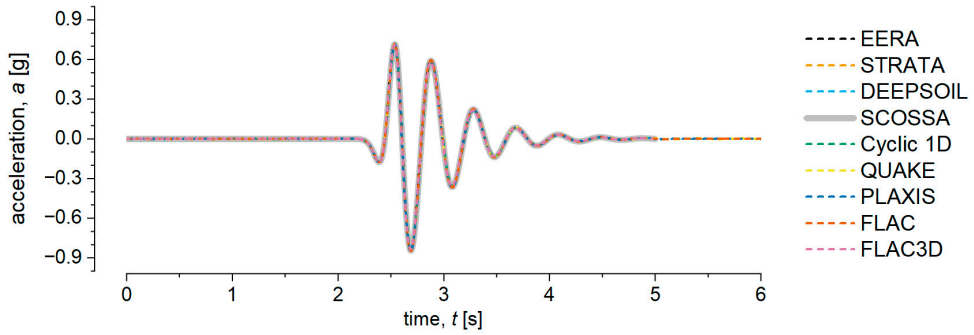

Figure 4. Surface accelerograms simulated with the nine adopted codes [48].

Similar results were also obtained in the framework of the international benchmark PreNoLin [34] in terms of surface to reference Fourier spectra ratio for an ideal soil column (Figure 5). Twenty-one collaborating teams evaluated twenty-three distinct numerical simulations, which incorporated more than ten different constitutive relationships [34]. The organizing committee categorized the participating codes into three main, non-mutually exclusive groups, based on the following key attributes: (1) the numerical implementation scheme employed; (2) the damping mechanism formulation across both low-strain and large-strain domains; and (3) the formulation governing cyclic hysteretic response. A preliminary validation stage (i.e., cross-comparison among numerical codes) on simplified, idealized scenarios was conducted using 23 different codes, including the SCOSSA code, which is designated as "T − 0" in Figure 5.

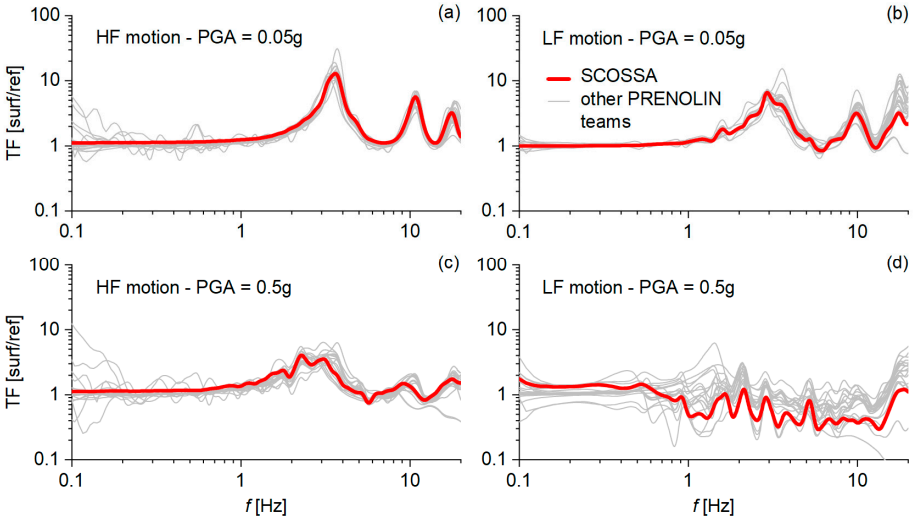

Figure 5. Comparison of the surface to reference Fourier spectra ratio for the nonlinear analyses using the high-frequency (HF) input motion (**a**) scaled to 0.5 m/s^2 and (**c**) scaled at 5 m/s^2, using the low-frequency (LF) input motion (**b**) scaled to 0.5 m/s^2 and (**d**) scaled at 5 m/s^2 [34].

3.2.2. Validation on Case Histories

The validation of the code's performance within the low-to-moderate strain regime is proposed by referencing a seismic instrumentation array situated near Sendai Port in Northeast Japan. This dataset was analyzed as part of the PreNoLin project [35]. The monitoring station comprises a surface-mounted accelerometer and a downhole geophone positioned at a 10.4 m depth. The array is established within a Holocene sedimentary formation, termed the "beach ridge", which is composed of marine-origin gravel and sand. This surficial deposit overlies the Pliocene Geba Formation, which constitutes the northern and eastern hills and is characterized by gravel stone, sandstone, tuff, tuffaceous siltstone, and lignite [22,35].

The Sendai array location was chosen as a validation benchmark for the PreNoLin project primarily because the subsurface layering is demonstrably near-horizontal (as confirmed by multiple Multichannel Analysis of Surface Waves—MASWtests), and the S-wave propagation vector of the selected seismic events is approximately vertical [19].

The upper stratum of the soil column consists of 1.25 m of loose gravel, which is underlain by 5.9 m of moderately dense fine sand. Below 7.15 m, a stiff slate formation is considered the seismic half-space. The phreatic surface is located at a depth of 1.45 m below the ground line. Downhole PS logging furnished the in situ shear wave velocity, while the stress–strain and strength properties were determined via laboratory testing of undisturbed samples [35,56].

The profile of shear wave velocity implemented in the simulations was obtained by calibrating the in situ measurements until they exhibited optimal convergence with the empirical surface-to-borehole transfer function derived from weak-motion seismic recordings.

Undisturbed sand specimens were collected from depths of 3.3 m and 5.4 m for the purpose of executing laboratory experiments. Both samples were subjected to cyclic undrained triaxial tests to characterize the pre-failure stress–strain attributes of the soil. Furthermore, the cyclic and static strength parameters were measured on the shallower sample through stress-controlled cyclic undrained and consolidated–drained triaxial tests, respectively [35,56]. The cyclic liquefaction resistance and pore pressure generation parameters were subsequently assigned to the fine sand layer based on the findings from the cyclic triaxial liquefaction tests.

In the one-dimensional (1D) analyses conducted using the SCOSSA code, the downhole acceleration records were applied as the input excitation. Consequently, a rigid bedrock condition can be postulated at a 10.4 m depth, coinciding with the downhole sensor's location. This is a standard assumption usually adopted when downhole recordings are available [35], due to the fact that the applied excitation is the resulting motion between the wave train directed toward the surface and the train of the downward reflected wave [48].

Conversely, the slate rock stratum positioned above the downhole sensor (spanning 7.0 m to 10.4 m) was modeled as a linear visco-elastic material with a uniform damping ratio of 1%. Six recorded input motions with three distinct PGA magnitudes ($\geq$0.06 g, 0.02–0.03 g, and $\leq$0.01 g) and two differing frequency content categories were considered.

Figure 6 provides a comparative assessment between the surface records and the simulated outcomes from the total stress analyses for high-frequency (Figure 6a) and low-frequency (Figure 6b) input motions. The findings are presented as spectral accelerations and time histories of acceleration, with both quantities normalized relative to the PGA captured at the surface.

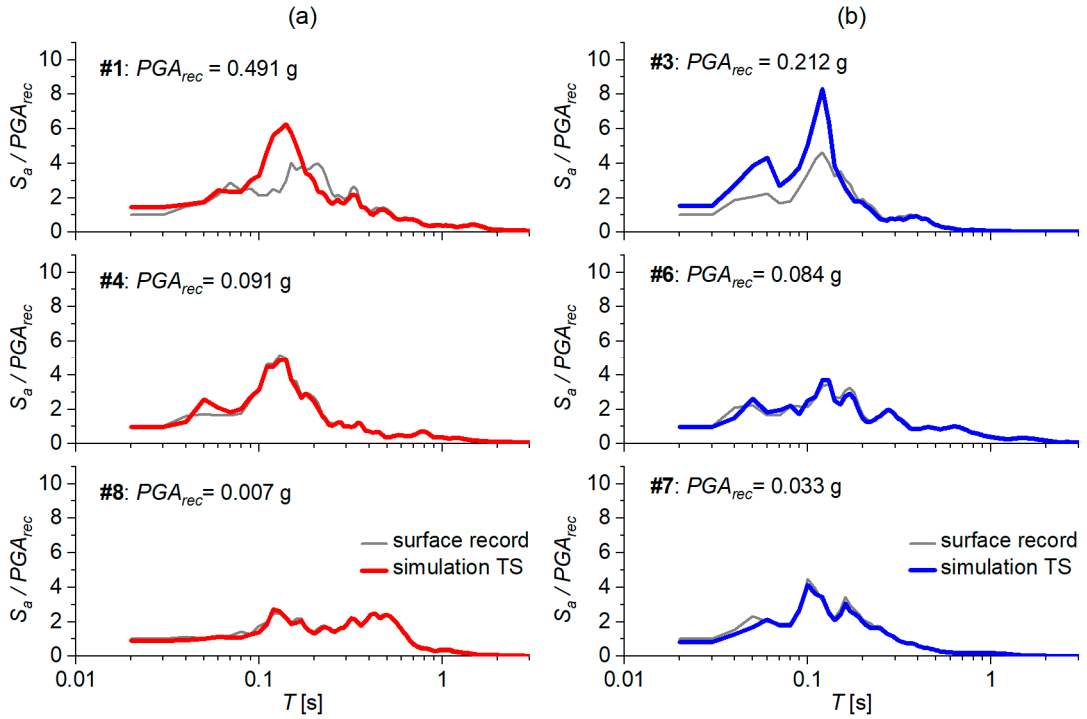

Figure 6. Sendai array: high-frequency (**a**) and low-frequency (**b**) input motions: surface acceleration response spectra recorded vs. those simulated with SCOSSA (RSL-TT) in total stress analyses [22].

4. Stick–Slip Model

The dynamics of the stick–slip model implemented in SCOSSA refer to the lumped mass system sketched in Figure 2 and then reproduced in Figure 7a, where a plastic slider is added for each layer, which is activated when the limit tension r is reached, thereby simulating layer breaking. The scheme can also include inclined layers to simulate an indefinite slope, or a frame overstructure modeled as an elementary oscillator [33]. Two stages of analysis can be identified: in the 'stick' phase, the potentially unstable mass cumulates vibrational kinetic energy, which is transformed into a frictional sliding mechanism during the 'slip' stage.

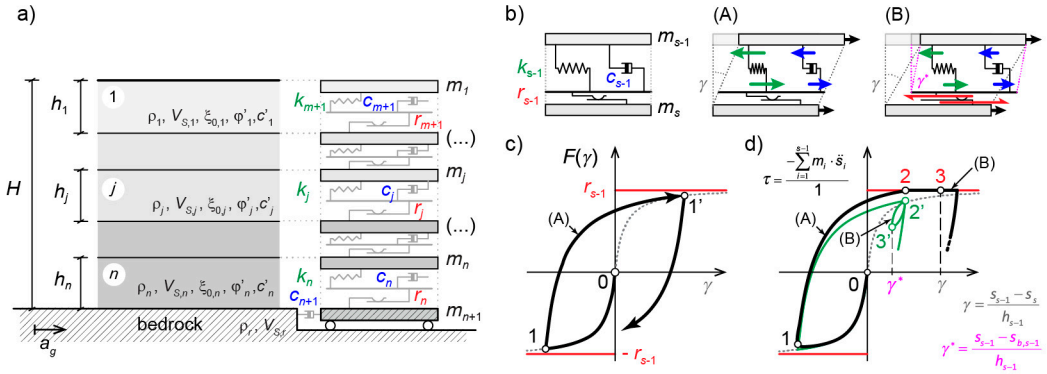

Figure 7. (**a**) MDOF system; (**b**) "Stick" and "slip" conditions in a two-mass system; (**c**) purely hysteretic behavior; (**d**) dynamic response of the system [33].

In the stick phase, the seismic response in terms of absolute displacements can be computed by integrating the system reported in Equation (1).

The vector of the applied forces depends on the input accelerogram, a_g, which can be applied as 'inside' or 'outcrop' motion and on the bedrock impedance.

The shear critical strength at a possible failure surface can be defined as $m_T\, a_y$, where m_T is the total mass above the failure surface, and a_y is the yield acceleration, typically computed by the limit equilibrium methods. The forces acting on the sliding interface (Figure 7) are:

$$-m_T\ddot{s}_s - \mathbf{1}^T\mathbf{M_s}\ddot{\mathbf{s}} \tag{16}$$

where the first is the inertial force induced by the absolute acceleration at the s-th layer, $\ddot{s}_s$, while the second results from the non-uniform relative acceleration profile, $\ddot{s}$, within the sliding mass, referred to $\ddot{s}_s$. $\mathbf{1}$ is the unity vector, while the subscript "S" indicates sub-matrices and sub-vectors with index from 1 to $(s-1)$ for the sliding part of the dynamic system.

The 'slip' conditions start when the inertia forces equal the resisting force corresponding to the product of the sliding mass and the yield acceleration, $m_T.a_y$. In such a case, the motion equation for the deformable mass above the sliding surface is:

$$\mathbf{M_s}\ddot{\mathbf{s}} + \mathbf{C_s}\dot{\mathbf{s}} + \mathbf{K_s}\mathbf{s} = -\mathbf{M_s}\mathbf{1}\left(\ddot{s}_s + \ddot{s}_0\right) \tag{17}$$

On the sliding surface, the equilibrium, during the slip, is governed by the condition

$$-m_T \cdot \left(\ddot{s}_s + \ddot{s}_0\right) - \mathbf{1}^T\mathbf{M_S} \cdot \ddot{\mathbf{s}} = m_T \cdot a_y \tag{18}$$

Substituting Equation (5) in Equation (4), the equation for the 'slip' conditions is

$$\mathbf{M}^*\ddot{\mathbf{s}}+\mathbf{C_S}\dot{\mathbf{s}}+\mathbf{K_S}\mathbf{s} = \mathbf{M_S}\ \mathbf{1}\ a_y \tag{19}$$

where **M*** is defined as

$$\mathbf{M}^* = \mathbf{M_S} - \frac{1}{m_T}\mathbf{M_S} \cdot \mathbf{1} \cdot \mathbf{1}^T\mathbf{M_S} \tag{20}$$

Solving Equation (6) in terms of nodal relative acceleration, $\ddot{\mathbf{s}}$, the sliding time histories of acceleration are computed from Equation (5) as:

$$\ddot{s}_0 = -a_y - \frac{1}{m_T} \cdot \mathbf{1}^T\mathbf{M_S} \cdot \ddot{\mathbf{s}} - \ddot{s}_s \tag{21}$$

The sliding displacement, s_0, is computed by integrating Equation (21) twice until the sliding velocity becomes equal to zero.

Figure 7b shows the performance of the constitutive model for the generic $(s-1)$th layer immediately above the sliding surface. The masses $s-1$ and s are connected by a nonlinear hysteretic spring (k_{s-1}), a viscous dashpot (c_{s-1}), and a plastic slider (r_{s-1}). Under static load, the MKZ model uses two relationships: $F_{bb}(\gamma)$ for first loading (e.g., $0 \rightarrow 1$ in Figure 7c) and $F_{ur}(\gamma)$ for unloading–reloading paths (e.g., $1 \rightarrow 1'$ in Figure 7c). The limiting strength is reached asymptotically when the MKZ model degenerates to the hyperbolic stress–strain relationship. In dynamic "stick" conditions (see pattern (A) and the corresponding point on the reloading curve in Figure 7d), the current value of shear stress, τ, is computed considering the dynamic equilibrium of the soil column (Equation (1)). As a consequence, the γ–τ relationship deviates from the purely hysteretic response (the dashed line in Figure 7d), shows rounded edges (point 1), and possibly reaches the limit strength (point 2), attaining "slip conditions" (pattern (B) in Figure 7b). Thereafter, the shear stress holds constant until the system accumulates plastic straining, while the hysteretic response of the spring results in a small unloading–reloading cycle (Figure 7d), induced by the application of modified Masing rules. Due to slippage, the subsystem above the sliding base is characterized by an actual value of the shear strain in a generic instant (indicated as γ^* in Figure 7b,d) lower than the total strain, γ.

Different options are implemented in the code to determine the position of the critical sliding surface, H_s, which can be either imposed before the analysis or automatically sought by identifying the layer where the slippage condition is tested for the first time.

The stick–slip was verified on a dam and a landslide case study, as reported in [3].

Figure 8 shows the results of a theoretical exercise modified from [33]. The soil is a normally consolidated, medium-plasticity clay layer (IP = 30%) with a unit weight equal to 19 kN/m^3 and a V_S profile that increases with depth (Figure 8a). The soil is characterized by cyclic hysteretic behavior defined by the Vucetic and Dobry curves [57]. The critical acceleration value of 0.017 g is depth-independent due to the combination of soil resistance, as defined by the Mohr–Coulomb failure criterion, and the gentle slope of the layers.

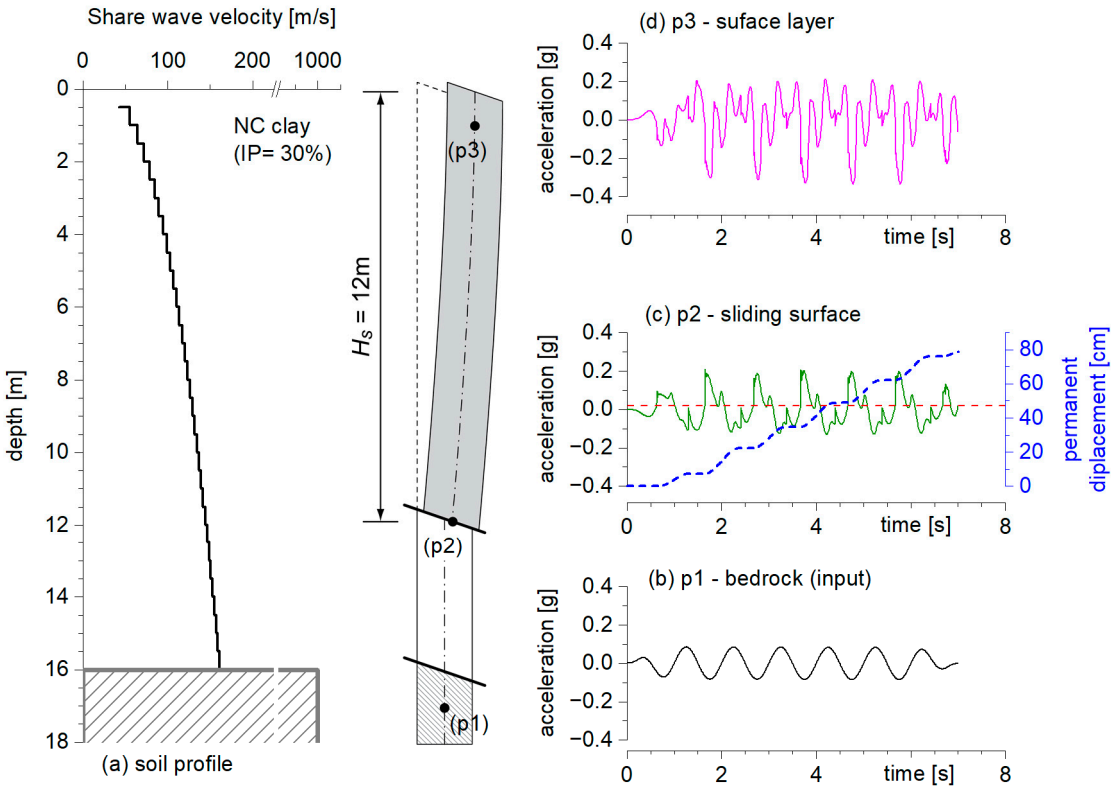

Figure 8. Example of results obtained for a virtual NC clay subsoil (**a**) with shear wave velocity profile increasing with depth subjected to a synthetic accelerogram (**b**) with frequency of 1 Hz: (**c**) acceleration (green line) and cumulated displacement (blue line) time histories obtained at sliding surface depth and (**d**) acceleration time history at surface layer (magenta line).

The input motion considered at the bedrock layer (p1 position in Figure 8b) is a sine wave with an amplitude of 0.1 g, frequency of 1 Hz, and duration of 7′ (equivalent to 7 cycles), with the first and last ones modulated in amplitude with two sigmoid laws. In Figure 8c,d, the results obtained at the first detected sliding surface depth (p2) and at the layer surface (p3) are shown. Details of the acceleration time history and cumulated displacements at the sliding surface layer are used to explain what occurs during the stick and slip phases.

At time t = 1.3 s, the unstable mass, which had accumulated about 5 cm from the previous slip phase, is in the stick condition until a new triggering of motion occurs at time 1.7 s (Figure 8c). During this lapse, the soil can respond to dynamic input with upstream instantaneous displacements. Starting at t = 1.7 s, a new slip stage with a gradual increase in displacement along the sliding surface occurs. As can be seen in the results shown in Figure 8c,d, the slip at the base of the column causes the freely oscillating system to respond

with a higher natural frequency than the non-sliding system. High-frequency oscillations resulting from numerical errors in the transition between phases are also observed. This oscillation propagates to the surface at the same frequency, displaying a clearly asymmetric amplitude signal.

Validation on Calitri Landslide

The considered case study focuses on a large-scale, complex landslide impacting the village of Calitri in Southern Italy, characterized by a dominant rotational failure mechanism that transitions into a mudslide near the toe as the mass approaches the left flank of the Ofanto river valley [58,59]. The failure envelope, as depicted in the main longitudinal cross-section [60], is approximately curvilinear, with a maximum basal depth of 94 meters and an average surface inclination of 10° (Figure 9a,b).

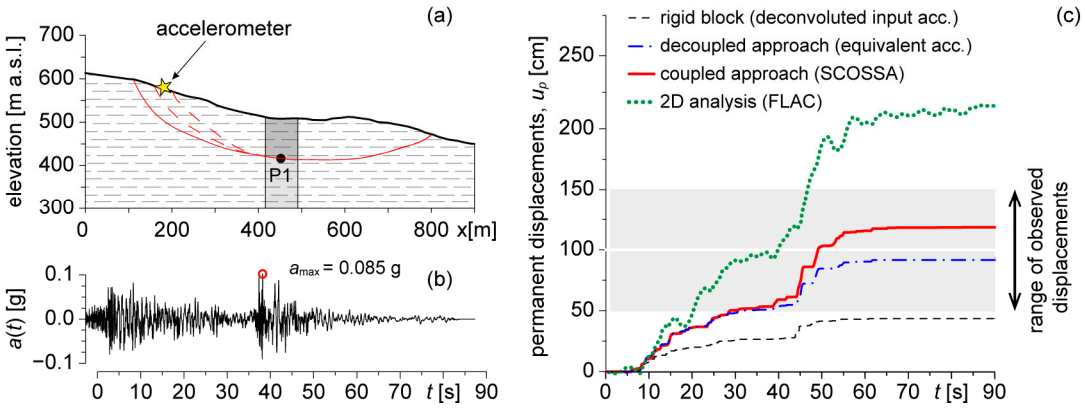

Figure 9. (**a**) Cross-section of Calitri landslide with the probable pre-seismic sliding surfaces reconstructed (red lines). (**b**) deconvoluted motion at 300 m a.s.l. (**c**) observed vs. cumulated displacements computed using the stick–slip model (red line) versus those predicted using FLAC 2D (green dotted line) and the rigid block method using the deconvoluted acceleration time history (black line) and the equivalent acceleration (blue line).

The slope movement was seismically triggered and reactivated by the two major mainshocks of the 23 November 1980, Irpinia earthquake (Mw = 6.9 and 6.2), resulting in incremental down-slope displacements ranging from 1 to 2 m [59]. Due to the sensor location at the landslide crown, the recorded strong-motion accelerogram was subject to stratigraphic amplification effects. Consequently, a reference acceleration time history for dynamic analysis was established via one-dimensional (1D) linear visco-elastic deconvolution through the layered subsoil profile, which was defined using available dynamic site characterization data [61,62]. For subsequent dynamic slope stability assessments, the input acceleration vector was projected onto the azimuth corresponding to the principal direction of movement. In the absence of direct piezometric readings contemporaneous with the seismic event, the hydrogeological regime for the dynamic analysis was approximated based on back-analysis interpolation [59], assuming a groundwater table depth of 5 m below the topographic surface.

To perform equivalent 1D dynamic analyses, an "equivalent infinite slope" paradigm was adopted, where the soil profile was chosen to correspond to either the maximum depth [63] or the mean depth [64] of the failure surface, necessitating the weighted averaging of the stiffness and strength parameters across the mobilized soil mass [3]. The computational efficacy of four distinct models—a rigid block model utilizing the reference and equivalent accelerograms, a 1D "stick-slip" model, and a 2D Finite Difference Method (FDM) analysis (FLAC code [65]), both incorporating soil deformability and strength coupling—was evaluated by comparing predicted cumulative horizontal displacements

against the observed displacement range [59]. The modeling results collectively demonstrate fair concurrence with empirical observations, although the degree of conservativeness scaled directly with model complexity: the rigid block approach yielded under-conservative estimates, the 2D FDM analysis proved over-conservative, and the decoupled and stick–slip methodologies provided well-balanced predictions (Figure 9c).

5. Liquefaction

The seismic response analysis of saturated soils is a complex process governed by two key phenomena: hysteresis and volumetric–distortional coupling. Hysteresis involves a reduction in shear modulus and increased damping, and volumetric–distortional coupling gives rise to irreversible plastic strain under high shear loads, which can lead to liquefaction in loose sands.

Although hysteretic effects are widely modeled, volumetric–distortional coupling remains a challenge. Two primary approaches are used to model pore water pressure variation:

- Decoupled approach: this method calculates excess pore pressure using semi-empirical relationships based on total stress analysis results.
- Coupled approach: this method performs effective stress dynamic analysis, calculating the time history of excess pore water pressure [66].

The coupled approach can be further divided into the following:

- Loosely coupled: predicts pore pressure using relationships combined with total stress constitutive models [67].
- Fully coupled: uses a plasticity-based constitutive model to simultaneously predict both stress–strain and pore pressure. Particularly popular in recent decades are multi-yield surface models (e.g., [51,68]) and bounding surface models (e.g., [69,70]).

For implementation in the code, a simplified stress-based pore water pressure model was considered. This model takes a loosely coupled approach, which makes it practical because it can handle irregular shear stress time histories directly, removing the need to calculate an equivalent number of uniform stress cycles—a common requirement for other simplified models (e.g., [71]). The model also avoids the complex parameter calibration required by more advanced plasticity-based approaches. This makes it a valuable tool in engineering practice, as it requires only a few easily calibrated parameters. The model also accounts for stiffness and strength degradation due to pore pressure build-up, considering the redistribution and dissipation of excess pore pressure based on one-dimensional consolidation theory.

The following reasons drove the choice of this model over the plethora of possible options: (1) the simplicity of the model, which is ruled by few analytical relationships; (2) the consistency of the model with the worldwide-accepted liquefaction framework based on the cyclic resistance curve of soils, i.e., stress-based approach; (3) the feasibility in implementing the model in a time domain integration algorithm; (4) the straightforward quantification of the model parameters through soil testing.

Concerning the last point, the calibration of the simplified pore water pressure model, originally developed based on the results of cyclic laboratory tests, was then expanded to the results of the cone penetration test, standard penetration test, and seismic dilatometer test [25,26]. However, these calibration procedures attempt to reproduce trends experimentally observed, without a rigorous connection with the soil mechanics theory. Additionally, different pore pressure curves belonging to the same soil but with different relative densities require independent calibrations of the model parameters.

Modifications to the basic numerical procedure of the code, as reported in Section 3, were necessary in order to implement the pore pressure generation and dissipation models.

Figure 10 shows the flowchart outlining the schematic algorithm adopted in the SCOSSA-PWP code for each time step.

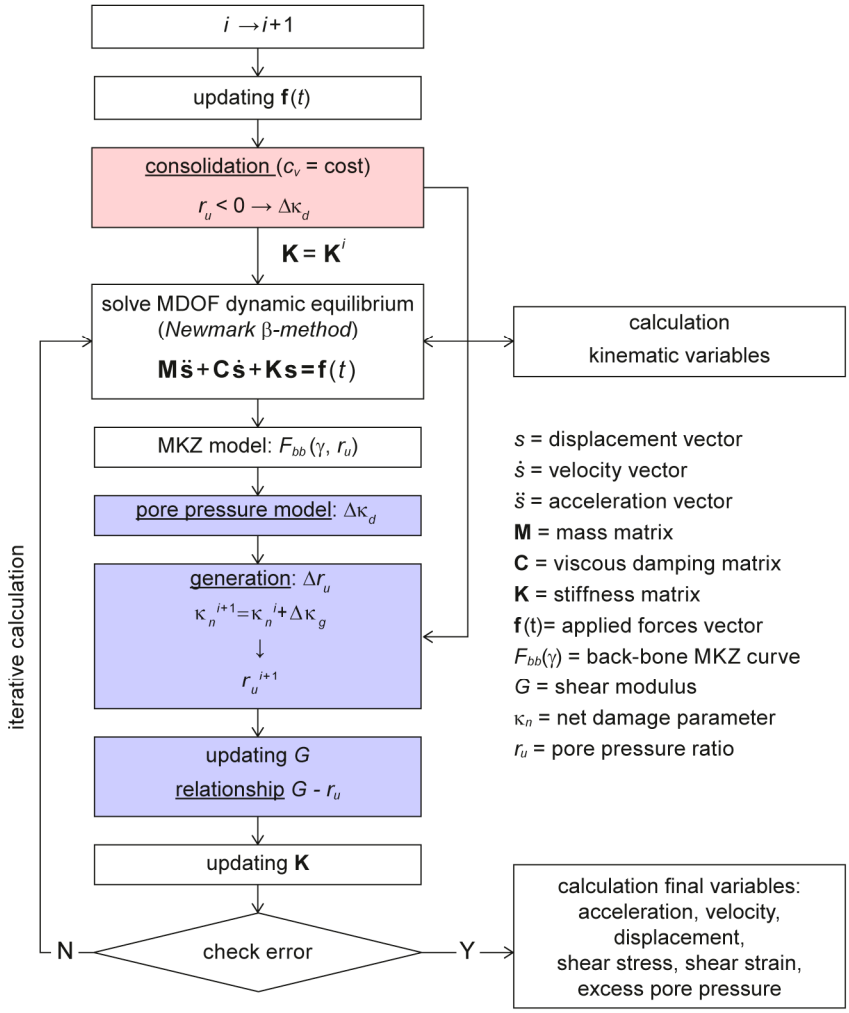

Figure 10. Flowchart for the numerical algorithm [22].

Novel modules have been integrated into the original SCOSSA algorithm, encompassing routines for consolidation (Figure 2c), pore water pressure generation, and shear modulus adjustment (indicated by the shaded boxes in Figure 10). A comprehensive explanation of these specific routines is reported in the following sections.

According to the flowchart in Figure 10, the vector of input forces, $\mathbf{f}(t)$, is initially updated for the i-th time step. During the same interval, a new distribution of pore water pressure along the soil profile is defined, starting from that evaluated at the previous time instant, with the consolidation coefficient held constant. The consolidation induces a decrease in the excess pore water pressure, with a negative variation in the pore pressure ratio, r_u; this variable is defined as the ratio between the pore pressure, Δu, and the initial effective stress of the soil, σ'_0 (vertical stress in cyclic simple shear or mean effective stress in different conditions).

The cyclic response model (Equation (13)) is modified by including the degradation index functions $\delta\tau$ and δ_G. The modulus degradation index function, δ_G, is defined as

$$\delta_G = \sqrt{1 - r_u} \tag{22}$$

while the corresponding stress degradation index function, $\delta\tau$, is given by

$$\delta_\tau = 1 - {r_u}^\mu \tag{23}$$

where μ is a constant that rules the sensitivity of the backbone curve to pore water pressure changes. Matasovic and Vucetic [42] determined μ for the stress–strain response obtained from strain-controlled cyclic simple shear tests on Californian sandy soils, ranging between 3.5 and 5. The same relationship between shear modulus and excess pore water pressure is widely used in other computer codes (e.g., D-MOD2000 [72]).

The above degradation index was also used to express the stress–strain relationship in unloading–reloading conditions, according to the relationship proposed by Moreno-Torres et al. [73]. As a consequence, Equations (13) and (14) are modified as follows:

$$F_{bb}(\gamma) = \frac{\delta_G\, G_0\, \gamma}{1 + \beta \left(\frac{\gamma}{\gamma_r} \frac{\delta_G}{\delta_\tau} \right)^{s'}} \tag{24}$$

$$F_{ur}(\gamma) = F^*(\gamma_m) \left[\frac{G_0\, \delta_G\, (\gamma - \gamma_c)}{1+\beta \left(\frac{\delta_G}{\delta_\tau} \right)^{s'} \left(\frac{\gamma - \gamma_c}{2\gamma_r} \right)^{s'}} - \frac{G_0\, \delta_G\, (\gamma - \gamma_c)}{1+\beta \left(\frac{\delta_G}{\delta_\tau} \right)^{s'} \left(\frac{\gamma_m}{\gamma_r} \right)^{s'}} \right] + \\ + \frac{G_0\, \delta_G\, (\gamma - \gamma_c)}{1+\beta \left(\frac{\delta_G}{\delta_\tau} \right)^{s'} \left(\frac{\gamma_m}{\gamma_r} \right)^{s'}} + \tau_c \tag{25}$$

5.1. PWP Model

The selected model belongs to the family of the endochronic models [74–79]. It is based on the "damage parameter", κ, that summarizes the effect of the cyclic variation of stress/strain on the undrained soil response. This parameter is an increasing variable of the loading history, directly correlated with the pore pressure accumulation as follows:

$$r_u = h(\kappa) \tag{26}$$

The pore pressure model also univocally correlates the normalized damage parameter, κ/κ_L, and the pore pressure ratio, r_u, through the polynomial [23]:

$$r_u = a \left(\frac{\kappa}{\kappa_L} \right)^b + c \left(\frac{\kappa}{\kappa_L} \right)^d \tag{27}$$

where a, b, c, and d are the curve-fitting parameters.

The use of the endochronic-based damage parameter, κ, avoids non-univocal criteria to convert irregular shear loading into an equivalent number of cycles [80], sometimes characterized by quite challenging procedures [81–83].

For a uniform load of amplitude CSR (i.e., the ratio between the modulus of the maximum shear stress, $|\tau_{max}|$, and the initial effective stress), κ is proportional to the number of cycles, N:

$$\kappa = 4N\, (\mathrm{CSR} - \mathrm{CSR}_t)^\alpha \tag{28}$$

An irregular shear loading history (Figure 9) is expressed as

$$\tau^*(t) = \frac{|\tau(t)|}{{\sigma'}_0} \tag{29}$$

The damage parameter can be calculated at every time instant as

$$\kappa(t) = \kappa_0 + d\kappa \tag{30}$$

where κ_0 is the damage cumulated at the last reversal point of the function (τ*–CSR$_t$) reached at the time instant, t. The parameter κ_0 can be defined as follows:

$$\kappa_0 = \begin{cases} \kappa(t-dt) & \text{if } \dot{\tau}^*(t) = 0 \quad \text{or } \tau^*(t) = \text{CSR}_t \\ \kappa_0(t-dt) & \text{if } \dot{\tau}^*(t) \neq 0 \quad \text{or } \tau^*(t) \neq \text{CSR}_t \end{cases} \tag{31}$$

i.e., κ_0 is a stepwise function assuming the value of the damage parameter gained at the time step ($t - dt$) every time the stress ratio is a local maximumor when τ* = CSR$_t$.

The increment in the damage parameter, $d\kappa$, in the time interval dt is

$$d\kappa = \begin{cases} 0 & \text{if } \tau^*(t) < \text{CSR}_t \\ [\tau_0^*(t) - \tau(t)]^\alpha & \text{if } \tau^*(t) \geq \text{CSR}_t \end{cases} \tag{32}$$

The damage function increases when τ* overtakes CSR$_t$, the threshold below which there is no pore pressure build-up (Figure 11).

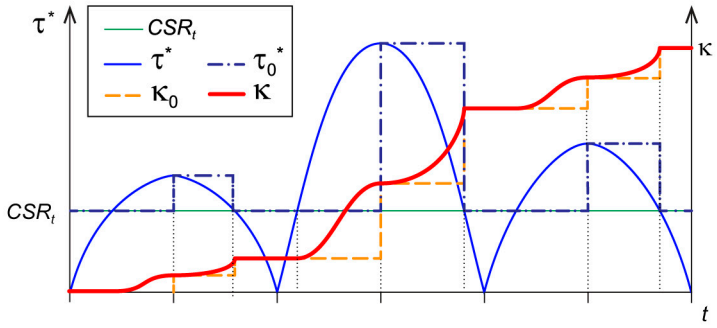

Figure 11. Accumulation trend of the damage parameter over time [23].

In the discrete time step analysis, it is possible to define the "generated damage" increment, $\Delta\kappa_{gen}$, as

$$\Delta\kappa_{gen} = \kappa_{i+1} - \kappa_i \tag{33}$$

The relationship for the cyclic resistance curve CRR, N_L is usually based on a power function [84–86]. The one considered in SCOSSA-PWP is that proposed by [78,79], which is rewritten as follows:

$$\frac{(\text{CRR} - \text{CSR}_t)}{(\text{CSR}_r - \text{CSR}_t)} = \left(\frac{N_r}{N_L}\right)^{\frac{1}{\alpha}} \tag{34}$$

where (N_r, CSR$_r$) is a reference point of the cyclic resistance curve, and the exponent α describes the dependency of the cyclic resistance on the number of cycles (Figure 12a).

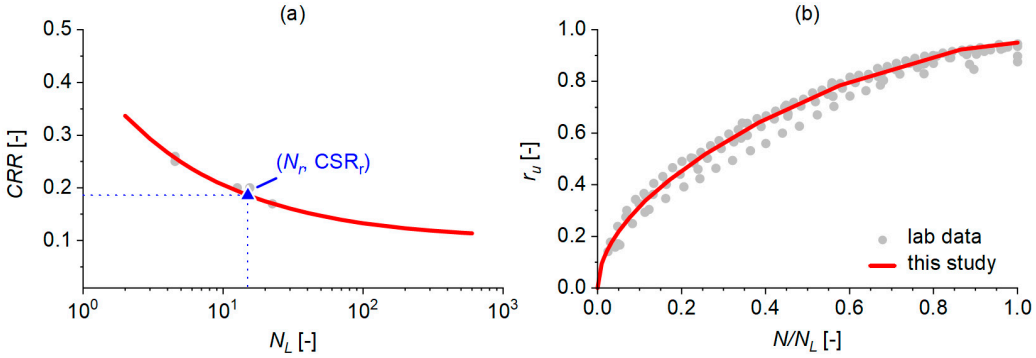

Figure 12. Cyclic stress ratio vs. number of cycles (**a**) and excess pore pressure ratio curve (**b**) for silty sand [22].

Combining Equations (34) and (28) for CSR equal to CRR, the damage parameter at liquefaction, κ_L, is expressed as follows:

$$\kappa_L = 4\ N_r(\mathrm{CSR}_r - \mathrm{CSR}_t)^{\alpha} \tag{35}$$

The relationship (35) shows that damage during liquefaction assumes a constant value depending on the parameters describing the cyclic resistance curve, α, CSR_r, and CSR_t. Therefore, any point on the cyclic resistance curve is associated with the same damage level, κ_L. In the N-CSR plane, different "iso-damage" curves can be drawn, representing, at any value of CSR, the number of cycles to reach damage corresponding to a given percentage of κ_L [23].

The normalized damage, i.e., the ratio between the damage, κ, and that evaluated at liquefaction, κ_L, is defined as follows:

$$\frac{\kappa}{\kappa_L} = \frac{4\ N(\mathrm{CSR} - \mathrm{CSR}_t)^{\alpha}}{4\ N_L(\mathrm{CSR} - \mathrm{CSR}_t)^{\alpha}} = \frac{N}{N_L} \tag{36}$$

Combining Equations (36) and (27), the normalized damage is equal to the ratio between the generic number of cycles and the number of cycles at liquefaction, N_L, as in the following equation (Figure 12b):

$$r_u = a\left(\frac{N}{N_L}\right)^{b} + (0.95 - a)\left(\frac{N}{N_L}\right)^{d} \tag{37}$$

Suggestions for calibrating model parameters using laboratory data are reported in [23,37], particularly concerning defining the asymptotic value of the cyclic resistance curve, CSR_t, which is often not clearly identifiable from experimental data.

One of the main challenges in performing effective stress analysis is calibrating a constitutive model that can simulate dynamic soil behavior under seismic loading. To address this issue, a calibration procedure was developed to define parameters for advanced constitutive models based on data from in situ tests, such as cone penetration tests (CPTs) and standard penetration tests (SPTs). Ntritsos and Cubrinovski [87] generated a dataset of cyclic resistance curves based on liquefaction triggering semi-empirical methods, and then used the dataset to calibrate an advanced constitutive model [88,89]. Following the above-mentioned approach, the calibration of simplified stress-based pore pressure models, which was initially based solely on cyclic laboratory test data, was extended to include results from field tests commonly used in engineering practice [25,26].

Figure 13 shows the CPT, SPT, and DMT-based charts for calibration of the PWP model parameters necessary for the definition of the cyclic resistance curve (Equation (34)).

In Figure 14, the pore pressure parameters are plotted as a function of the fines content and relative density. More recently, de Cristofaro et al. [90] showed the dependency of the mechanism of excess porewater pressures on stress history, stress state, and stiffness of soils by using two key parameters, ψ and λ, derived from steady-state theory. Consequently, the pore pressure parameters (Equation (37)) were correlated with the state parameters for two pyroclastic soils, experimentally investigated using cyclic triaxial tests.

Table 3 summarizes the parameters of the PWP model and the procedure used for their definition based on the results of soil investigations and laboratory or in situ tests.

Table 3. Definition of the parameters for the PWP model.

Parameter	Source	Calibration
Cyclic resistance curve parameters (α, CSR_r, CSR_t)	Cyclic resistance curve from laboratory tests (e.g., cyclic simple shear; stress-based cyclic triaxial)	Nonlinear multi-regression analysis of the experimental data points to fit Equation (34)
Pore pressure ratio coefficients (a, b, and d)	Excess pore pressure ratio vs. normalized number of cycles from laboratory tests (e.g., cyclic simple shear; stress-based cyclic triaxial)	Nonlinear multi-regression analysis of the experimental data points to fit Equation (37)
Cyclic resistance curve parameters (α, CSR_r, CSR_t)	CPT	Using the charts (a1, a2, a3) in Figure 13 with SPT data
Cyclic resistance curve parameters (α, CSR_r, CSR_t)	CPT	Using the charts (b1, b2, b3) in Figure 13 with CPT data
Cyclic resistance curve parameters (α, CSR_r, CSR_t)	DMT	Using the charts (c1, c2, c3) in Figure 13 with DMT data
Pore pressure ratio coefficients (a, b, and d)	SPT, CPT, DMT	Using the charts in Figure 14 with relative density and fines content estimated via correlation with SPT or CPT of DMT results

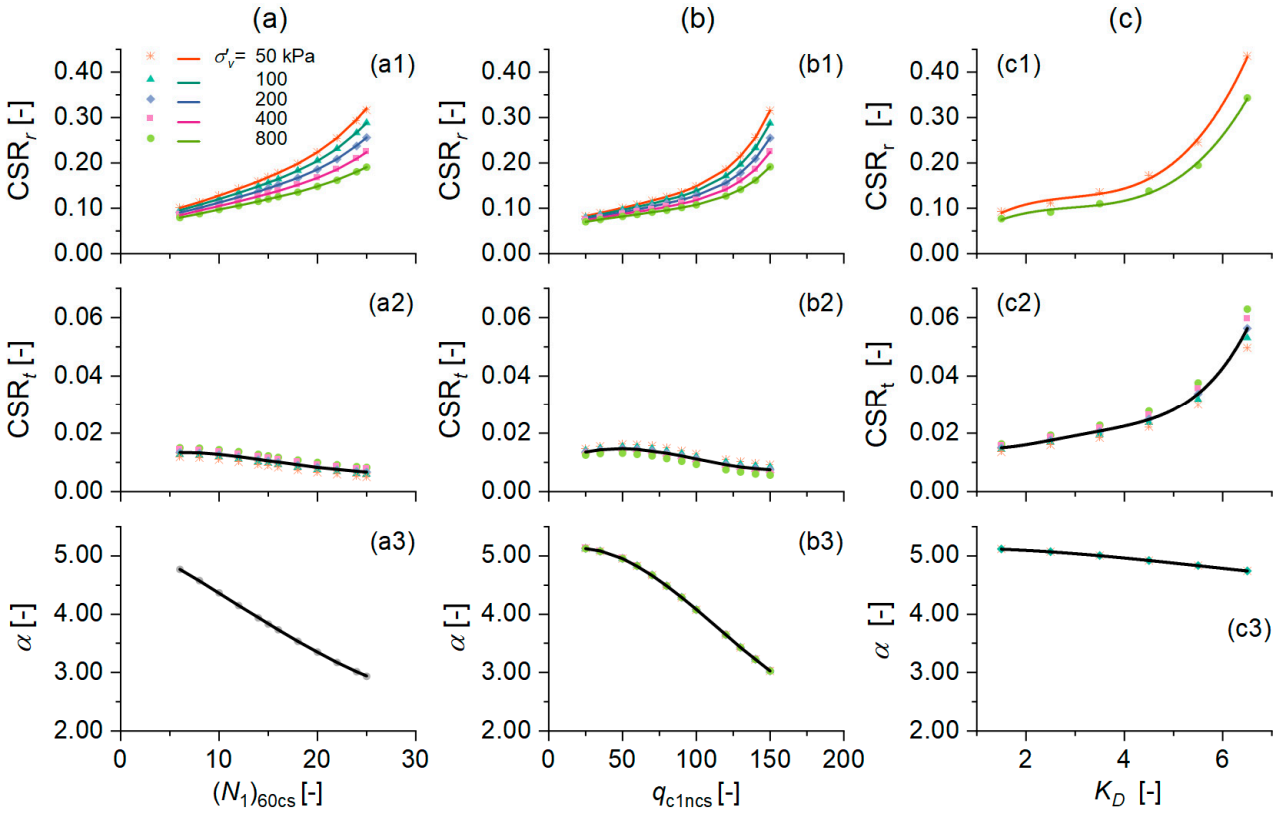

Figure 13. SPT-, CPT-, and DMT-based charts for calibration of the cyclic resistance curve parameters [25,26]: CSR_r parameter as a function of (**a1**) $(N_1)_{60cs}$, (**b1**) q_{c1ncs} and (**c1**) K_D; CSR_t parameter as a function of (**a2**) $(N_1)_{60cs}$, (**b2**) q_{c1ncs} and (**c2**) K_D; α parameter as a function of (**a3**) $(N_1)_{60cs}$, (**b3**) q_{c1ncs} and (**c3**) K_D.

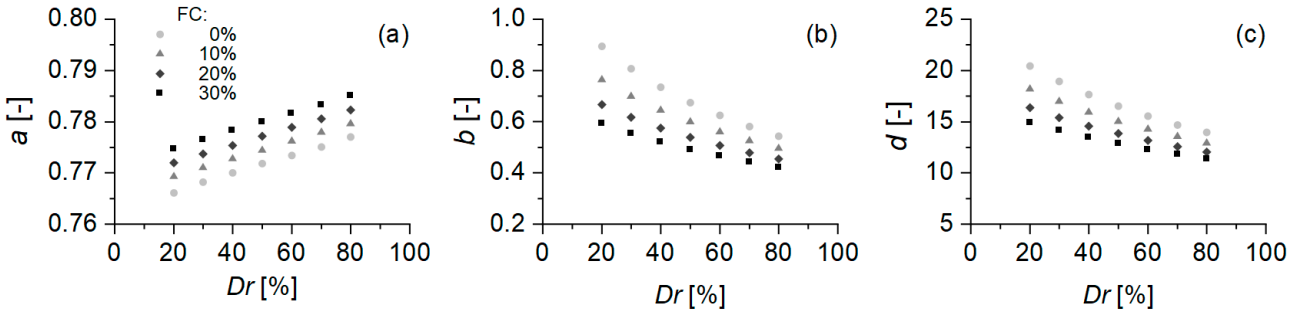

Figure 14. Parameters of the pore pressure model (**a**) *a*, (**b**) *b* and (**c**) *d* as a function of the fines content (FC) and relative density (Dr) [25].

5.2. Review of Applications and Case Studies

The performance of "SCOSSA PWP" in predicting pore water pressure build-up and dissipation has been validated against data from seismic centrifuges [22,27,28] and instrumented field sites [22,25,27]. Comparisons with more complex codes on real and ideal cases [29,30], including the numerical benchmark LICORNE [91], have also been performed.

Furthermore, post-analysis results have been used to predict both horizontal displacements and post-consolidation settlements in real-world case studies, with estimates aligning well with observed damage [27,31,92]. Further applications to case studies have been performed to investigate the effect of unsaturated soils on cyclic strength [28,93] and to investigate possible sources of damage at liquefaction sites, such as Pieve di Cento [94].

To illustrate the types of analyses the code can handle, total undrained effective stress analyses are presented below. Specifically, the Sendai and Port Island vertical array case studies illustrate analyses of totally undrained effective stress. The dissipation and redistribution of excess pore water pressure are challenging phenomena to analyze in a real case study, so several physical models have been developed in centrifuge tests to gain insight into liquefaction mechanisms [95–100]. These tests have been used as a reference for validation of advanced constitutive models and codes [101,102]. Similarly, the code's performance in partially drained effective stress analyses is shown in the following section for the numerical simulations of centrifuge tests.

5.2.1. Validation on Sendai Case Study

The simulations reported in Section 3.2 were repeated under effective stress conditions. Although the entire set of input motions listed in Section 3.2 was considered, excess pore pressure was only triggered for records #1 and #3 (i.e., those with the highest PGAs, at 0.257 and 0.062 g, respectively). For all other input motions, the results of the effective stress analyses coincided with those shown above.

The effective stress analysis results for input motions #1 and #3 are shown in Figure 15, along with the recorded data and the results of the total stress analyses. The effective stress analyses simulate ground motion at the surface, with satisfactory replication of the predominant periods and maximum spectral accelerations.

The Sendai analyses validate the code's ability to predict site response and pore-pressure build-up in a fully undrained, liquefiable reclaimed deposit under a wide range of seismic intensity, i.e., from very low to high shear strain levels.

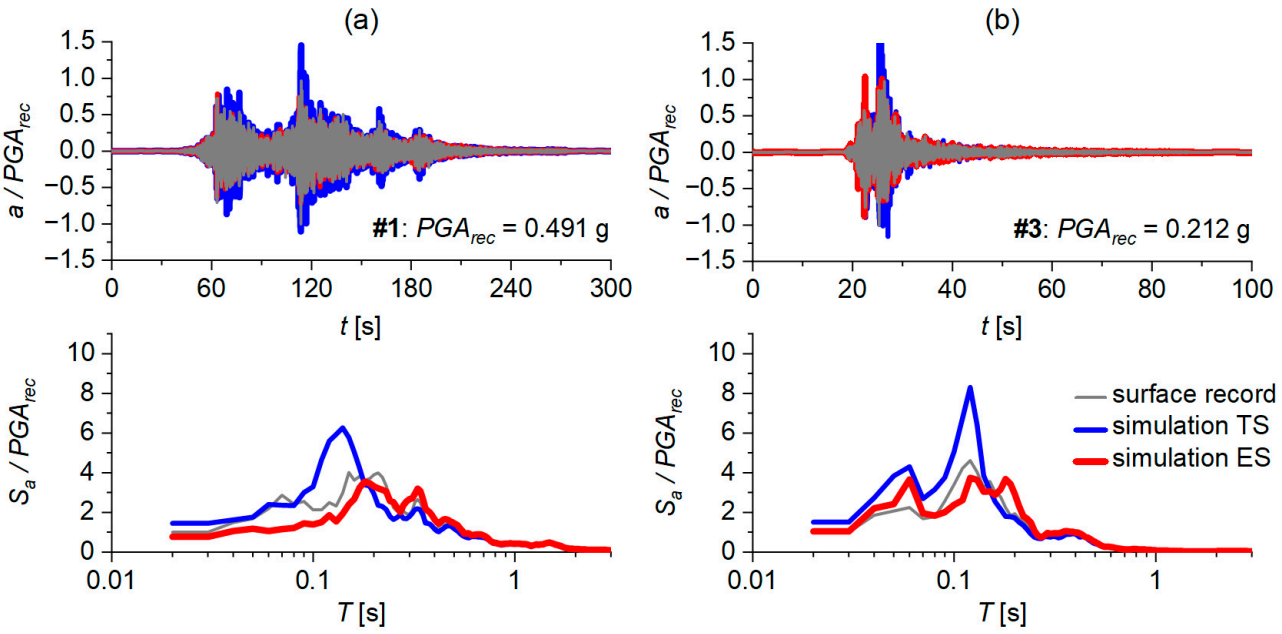

Figure 15. Strongest (**a**) #1 and (**b**) #3 input motions of the Sendai array: surface acceleration response spectra recorded vs. those simulated by total (TS) and effective stress (ES) analyses [22].

5.2.2. Validation on Port Island Case Study

Port Island is a well-known example of liquefaction on reclaimed ground used by several research groups to validate liquefaction models [103–107]. Following the 1995 earthquake, various areas of the artificial island exhibited clear signs of liquefaction [108]. Port Island was the first man-made island to be built in Osaka Bay, south of Kobe City. The construction of the island was undertaken in two phases. The initial phase of reclamation utilized soil comprising decomposed granite, known as "Masado", whereas the southern reclamation employed sandstone, mudstone, and tuff.

The 1995 Hyogoken-Nanbu earthquake, which had a moment magnitude of 6.9 (7.1 according to the Das Magnitude Scale proposed by [109]), impacted the southern portion of Hyogo Prefecture. The hypocentral depth was determined to be 14.3 km below sea level, with the epicenter located 15 km north of Awaji Island. Liquefaction occurred extensively throughout the island. The mean settlement was found to be 20 cm, with peak values exceeding 50 cm in the areas most severely impacted. According to the testimony of witnesses, the process of ejection of liquefied materials on Port Island continued for approximately one hour in the aftermath of the earthquake. The "Masa" or "Masado" soil constitutes the superficial sandy layer, composed of decomposed granite transported from the nearby Rokko Mountains, overlying a Holocene silty clay layer. Below these layers, alternate layers of Pleistocene gravel and clay can be found. The Masado soil is well graded, containing approximately 55% gravel and exhibiting a relative density of 47% for the silty sand portion of undisturbed samples. The groundwater table is located at a depth of 3 m below the surface, while the bedrock is situated at a depth of 16 m.

Figure 16 shows the normalized shear modulus, G/G_0, and damping, D, curves used in the investigation. The shear modulus reduction and damping curves reported in Figure 16h were used to capture Non-Masing behavior. The input motion was provided at the base of the soil column.

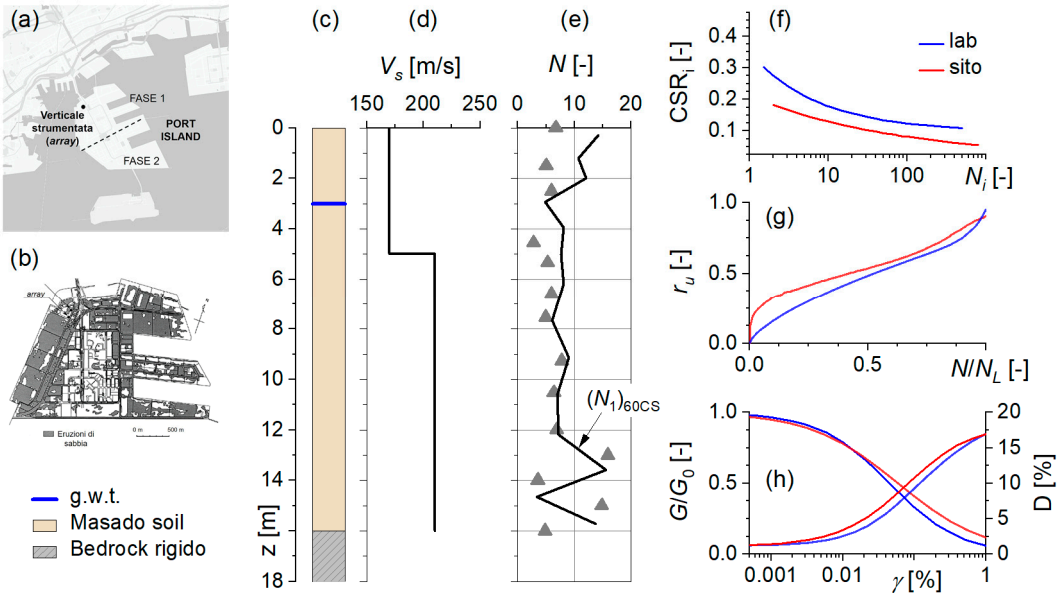

Figure 16. Port Island vertical array: (**a**) plan position of the site; (**b**) observed damage following 1995 Hyogoken-Nanbu earthquake; (**c**) stratigraphic column; (**d**) shear wave velocity profile; (**e**) SPT test results (gray symbols) and normalized value (black line); (**f**,**g**) curves for the PWP model; (**h**) hysteretic behaviour of the soil.

Since the ejection of liquefied materials on Port Island persisted for about an hour [108], the dissipation of the excess pore water pressure was not considered during the time of the shaking, and the analyses were performed in totally undrained conditions.

The simulation of the soil response at the array site was performed with SCOSSA and DEEPSOIL [43]. For the two codes, the same parameters were considered, except for the pore water pressure model. In DEEPSOIL, the Dobry/Matasovic model was selected, and the parameters were calibrated according to the Carlton [110] procedure, as detailed by Paul et al. [111].

This Dobry/Matasovic model for sand was initially proposed by Dobry et al. [112], and it was updated by various researchers [113]. The formula below was used to estimate excess pore water pressure:

$$r_u = \frac{p\, f\, N_{eq}\, F\left(\gamma_c - \gamma_{tvp}\right)^s}{1 + f\, N_{eq}\, F\left(\gamma_c - \gamma_{tvp}\right)^s} \tag{38}$$

where N_{eq} is the equivalent number of cycles for the most recent reversal of strain, and it is set equal to the number of cycles for loading. Since the cycle number is irregular for strain cycles, N_{eq} is determined at each strain using a 0.5 increment. The volumetric threshold shear strain is γ_{tvp}. When the shear strain level exceeds the threshold shear strain value, the excess pore water pressure is different from zero.

Vucetic and Dobry [113] introduced the parameter f for the purpose of modeling model cyclic loading in various dimensions. The value of f is equal to 1 in 1D motion and 2 for 2D motion. The fitting curve parameters, F, s, and p, are calibrated by using the results of laboratory tests. However, empirical correlations for the curve fitting parameters F and s for sands were proposed by [110] according to the following expressions:

$$F = 3810\, V_s^{(-1.55)} \tag{39}$$

$$s = (\mathrm{FC} + 1)^{0.1252} \tag{40}$$

where FC is the fines content (in percentage), and V_s is the shear wave velocity in m/s.

The same column was analyzed by [114] adopting the advanced constitutive model PM4Sand [115] for the modeling of the Masado soil, starting from the calibration work performed in [116]. The PM4Sand constitutive model requires three primary input parameters: the apparent relative density D_R, the shear modulus coefficient Go, and the contraction rate parameter hpo. D_R was estimated based on standard penetration test (SPT) results. Go governs the small-strain shear stiffness and was calibrated against shear wave velocity measurements. hpo controls the soil's contractiveness and, consequently, its cyclic strength; this parameter was iteratively calibrated to achieve the target cyclic strength documented in Figure 15. All secondary model parameters were maintained at their default values. Further details on the model and calibration procedure are omitted here for the sake of brevity, but the reader can find them in [114]. The synthesis of the comparison among the main features of the three considered codes is briefly summarized in Table 4.

Table 4. Comparison among the three considered computer codes.

Computer Code	Constitutive Model	Effective Stress Approach	Required Parameters	Calibration	Computational Demand
SCOSSA	MKZ + PWP	Loosely coupled	3 MKZ (β, s, and γr) + 6 PWP (α, CSRr, CSRt, a, b, d)	straightforward	Low
DEEPSOIL	MKZ + Vucetic and Dobry [97]	Loosely coupled	3 MKZ (β, s, and γr) + 6 PWP (γ_{tvp}, f, F, s, and p)	straightforward	Low
FLAC	PM4Sand [115]	Fully coupled	3 primary parameters (Go, D_R, h_{po})	Trial and error for h_{po}	High

The results of the effective stress analyses in terms of acceleration response spectrum are compared in Figure 17 for the NS component.

The Port Island analysis validates the code's ability to predict site response and pore-pressure build-up in a fully undrained, liquefiable reclaimed deposit under a severe earthquake scenario.

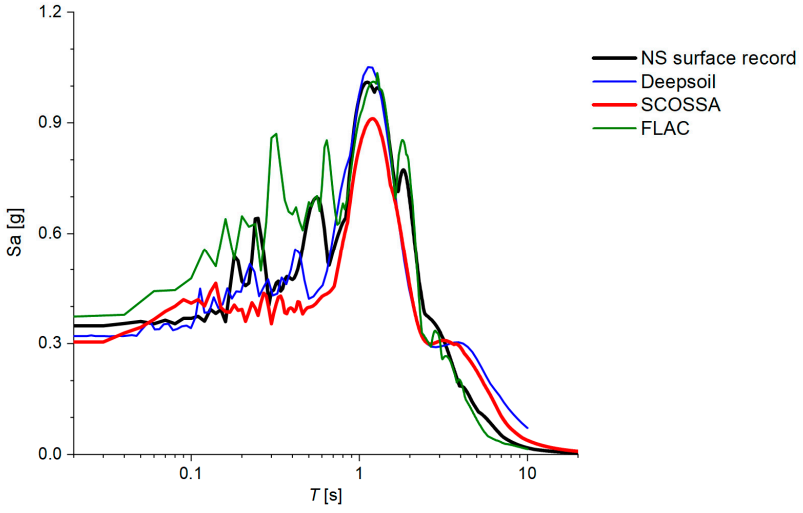

Figure 17. Acceleration response spectra for the NS component of the 1995 Kobe earthquake as obtained at the surface of the Port Island vertical array.

5.2.3. Validation Against Centrifuge Test Results

The first centrifuge experiment considered in the simulation is Centrifuge test No. 1 from the VELACS project [117]. The test was conducted to model a one-dimensional (1D) free-field liquefaction scheme, utilizing a uniform, fully saturated layer of Nevada sand with a relative density of approximately 40% and a total unit weight of 19.36 kN/m^3. The sand layer was housed in a laminar box composed of 30 stacked aluminum frames with roller bearings, allowing the box to deform congruently with the soil, thus simulating the seismic response of a semi-infinite sand layer. The model was tested under a centrifuge acceleration of 50 g while being excited horizontally at the base with a target prototype accelerogram (Figure 18d); vertical acceleration was negligible. Instrumentation, including horizontal (AH) and vertical (AV) accelerometers and piezometers (P), allowed for continuous monitoring of soil motion and the development of excess pore water pressures, which were confirmed to exhibit 1D behavior based on essentially identical time histories recorded at the same elevations (Figure 18a).

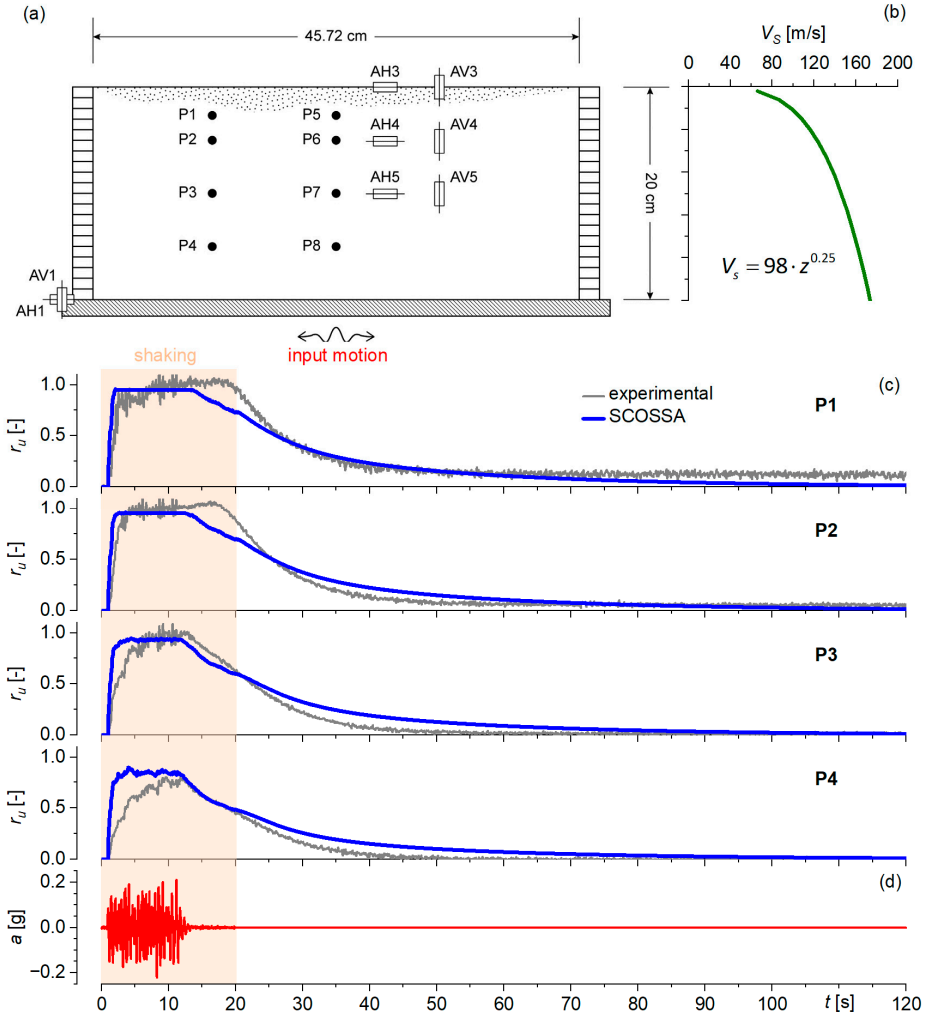

Figure 18. (**a**) Cross-section of the centrifuge laminar box, (**b**) V_S profile, (**d**) reference input motion (red line), and (**c**) recorded (grey lines) and computed (blue lines) pore pressure time histories until the end of the dissipation, as reported in [22].

The model consisted of a 10 m thick uniform sand layer (20 cm on the prototype scale) with an impervious base and a groundwater table at the surface. The dynamic properties of the sand were defined using resonant column tests, linking small-strain stiffness.

The cyclic resistance and pore pressure relationships were also determined from laboratory tests [118]. A key aspect of the numerical simulation was the use of a unit weight of 25.05 kN/m^3 to account for the inertia of the test frames. The consolidation coefficient was determined by matching post-shaking pore pressure dissipation curves, avoiding uncertainties from small-scale lab tests.

The results of the simulation, shown in Figure 18, successfully predicted the pore pressure response. At depths of 1.45 m (P1), 2.6 m (P2), and 5 m (P3), the soil was predicted to liquefy, reaching a pore pressure ratio of 0.95 after 2 seconds of shaking. The model also accurately predicted that liquefaction would not occur at a 7.5 m depth (P4). Both the simulation and test results showed the typical pattern of initial pore pressure build-up followed by dissipation from the bottom up. However, the simulation showed maximum pore pressures occurring earlier at greater depths than in the actual test, possibly due to the model assuming a uniform density. The simulation also showed dissipation starting simultaneously at all depths, whereas the test results showed a delay in dissipation closer to the surface.

To demonstrate the capacity of the code to accurately predict the development of pore pressure even in conditions far from liquefaction, the simulations of the centrifuge tests on Ticino and Pieve di Cento sands as reported in [28] are also presented in Figure 19.

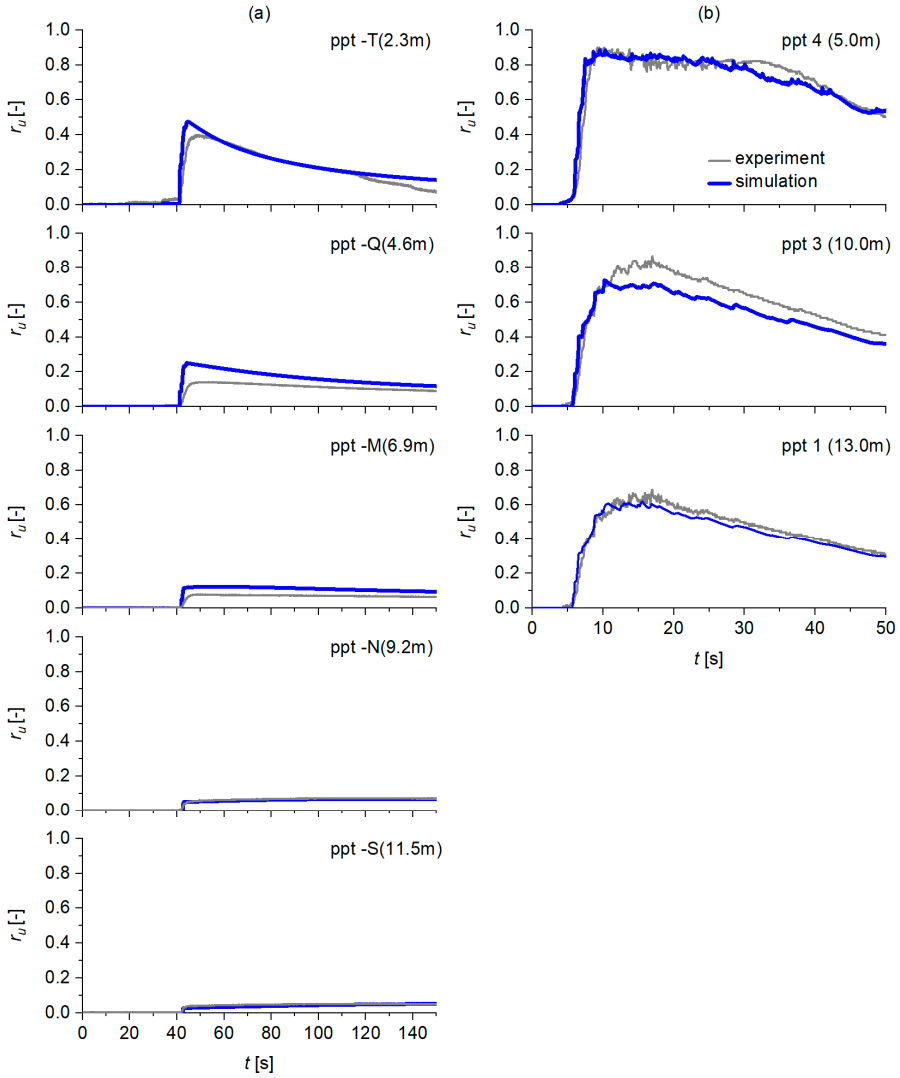

Figure 19. Recorded vs. simulated excess pore pressure time histories on a (**a**) saturated and (**b**) partially saturated sand (Sr = 88%) tested in centrifuge, as reported in [28].

The simulation of centrifuge tests validates the code's ability to predict site response and pore-pressure build-up in a partially drained, liquefiable sand deposit from a low to severe earthquake scenario.

5.3. Detected Limitations

Several limitations or drawbacks can be detected in version 1 of the code:

- The stick–slip model is validated against a few case studies and needs to be extended. To the best of the authors' knowledge, there are no other codes where the stick–slip model is implemented. As a consequence, the lack of comparison and verification in real cases implies that caution should be exercised in using the results.
- The numerical errors detected in the stick–slip scheme can be substantial. As a consequence, the results are suggested to be compared with simpler approaches before reaching a conclusion.
- The proposed method for liquefaction is not able to properly model the actual soil behavior after the triggering of liquefaction. Similarly to the codes which incorporate a loosely coupled approach reported in Table 1, the model does not account for the dilatative behavior of the soil observed after liquefaction triggering. This implies that the results are not adequate if the after-triggering behavior wants to be reproduced, and it is necessary to move to advanced constitutive models, such as those implemented in CYCLIC 1D [51], able to perform a fully coupled analysis.
- The PWP model calibration on in situ tests is based on the cyclic resistance curve analytically described by an exponential law, so the parameter CSR_t tends to be zero. This implies that the in situ-based PWP model calibration is less effective when the range of considered seismic action is around low CSR values, i.e., moderate- to low-intensity earthquakes. In the latter cases, the correct identification of the volumetric threshold strain and related CSR_t can be obtained with specific laboratory tests.
- The calibration of the PWP model for a specific relative density of the soil cannot be extended to a different relative density, but a new calibration of the model parameters is necessary even though the soil is the same. This makes the calibration process a bit long and repetitive compared to other models, where soil calibration is independent of the relative density.
- The boundary conditions for dissipation and redistribution of excess pore water pressure are imposed only at the base of the soil profile. This limitation constrains the cases that can be analyzed. The same limitation can be detected in other 1D codes, such as DEEPSOIL [43], while the use of more complex codes is necessary.
- Validation of soil models tested in centrifuge tests is limited to models with a single layer of sand, while layered configurations have not yet been considered. This implies that results from layered soil configurations should be used with caution because of the lack of specific validation.

6. Conclusions and Future Developments

The computer code SCOSSA version 1.0 has been demonstrated to be a valuable tool for the prediction of the seismic response of horizontally layered deposits across the entire range of shear strain levels, from very low to liquefaction.

The model and code were subjected to preliminary testing on an ideal soil profile with varying drainage conditions and subsequently validated by comparing predictions with centrifuge test results and seismic motions recorded at well-documented array stations.

The strong correspondence observed between numerical outcomes and experimental results underscores the reliability of the model incorporated within the code, despite the simplicity of the proposed approach.

In the short term, the code is undergoing re-engineering to improve its handling of input and output data. At the conclusion of this phase, a new version of the code will be released for free. It is anticipated that version 2.0 of the code will rectify or mitigate the aforementioned drawbacks. In detail, the primary goal for v2.0 is the optimization of the adopted algorithm to substantially reduce the computation time and an improvement in the software interface to make it more user-friendly and freely accessible. The boundary conditions will be modified to allow the drainage of excess pore water pressure at different depths of the soil column. Validation of the new version on layered soil configurations, as tested in centrifuge tests, is also planned to verify the above upgrade. Calibration guidelines and new protocols for the definition of the input data for the analysis are also currently in progress.

In the long term, there is a proposal for a loosely coupled formulation to be integrated with the stick–slip model. This would facilitate the prediction of permanent deformation mechanisms.

Author Contributions: Conceptualization, A.C. and G.T.; methodology, A.C. and G.T.; software, A.C. and G.T.; validation, A.C. and G.T.; formal analysis, A.C. and G.T.; investigation, A.C. and G.T.; resources, A.C. and G.T.; data curation, A.C. and G.T.; writing—original draft preparation, A.C.; writing—review and editing, A.C. and G.T.; visualization, A.C. and G.T.; supervision, A.C. and G.T.; project administration, G.T.; funding acquisition, A.C. and G.T. All authors have read and agreed to the published version of the manuscript.

Funding: We acknowledge financial support under the National Recovery and Resilience Plan (NRRP), Mission 4, Component 2, Investment 1.1, Call for tender No. 1409 published on 14 September 2022 by the Italian Ministry of University and Research (MUR), funded by the European Union—NextGenerationEU–Project Title "RI-SCOSSA 2.0—Renovation and Improvement of Seismic COde for Stick-Slip Analyses"—CUP P20228HN9M Grant Assignment Decree No. 1385 adopted on 1 September 2023 by the Italian Ministry of Ministry of University and Research (MUR).

Institutional Review Board Statement: Not applicable.

Informed Consent Statement: Not applicable.

Data Availability Statement: The data presented in this study are available upon request from the corresponding author.

Conflicts of Interest: The authors declare no conflicts of interest.

Abbreviations

The following abbreviations are used in this manuscript:

PWP	Pore Water Pressure.
SCOSSA	Seismic Computer Code for Stick–Slip Analysis.
CRR	Cyclic Resistance Ratio.
CSR	Cyclic Stress Ratio.
PreNoLin	Prediction of Non-linear Soil Behaviour.
PGA	Peak Ground Acceleration.
MASW	Multichannel Analysis of Surface Waves.
MDOF	Multiple-Degree-Of-Freedom.

References

1. NTC. Aggiornamento Delle Norme Tecniche per le Costruzioni. 2018. Available online: https://www.gazzettaufficiale.it/eli/id/2018/2/20/18A00716/sg (accessed on 21 December 2025).
2. Rathje, E.M.; Bray, J.D. Nonlinear coupled seismic sliding analysis of earth structures. *J. Geotech. Geol. Eng.* **2000**, *126*, 1002–1014. [CrossRef]

3. Tropeano, G.; Chiaradonna, A.; d'Onofrio, A.; Silvestri, F. An innovative computer code for 1D seismic response analysis including shear strength of soils. *Geotechnique* **2016**, *66*, 95–105. [CrossRef]
4. Cubrinovski, M.; Rhodes, A.; Ntritsos, N.; Van Ballegooy, S. System response of liquefiable deposits. *Soil. Dyn. Earthq. Eng.* **2018**, *124*, 212–229. [CrossRef]
5. Dhakal, R.; Cubrinovski, M. Liquefaction response of reclaimed soils from effective stress analysis. *Soils Found.* **2025**, *65*, 101677. [CrossRef]
6. Hutabarat, D.; Bray, J.D. Effective stress analysis of liquefiable sites to estimate the severity of sediment ejecta. *J. Geotech. Geoenviron. Eng.* **2021**, *147*, 4021024. [CrossRef]
7. Bassal, P.C.; Boulanger, R.W.; Dejong, J.T. System Response of an Interlayered Deposit with Spatially Distributed Ground Deformations in the Chi-Chi Earthquake. *J. Geotech. Geoenviron. Eng.* **2022**, *148*, 05022004. [CrossRef]
8. Bassal, P.C.; Boulanger, R.W. System Response of an Interlayered Deposit with Spatially Preferential Liquefaction Manifestations. *J. Geotech. Geoenviron. Eng.* **2021**, *147*, 05021013. [CrossRef]
9. Boulanger, R.W.; Bassal, P. 9th Ishihara lecture: Effects of subsurface heterogeneity on liquefaction-induced ground deformation during earthquakes. *Jpn. Geotech. Soc. Spec. Publ.* **2024**, *10*, 1–27. [CrossRef]
10. Hutabarat, D.; Bray, J.D. Estimating the severity of liquefaction ejecta using the cone penetration test. *J. Geotech. Geoenviron. Eng.* **2022**, *148*, 4021195. [CrossRef]
11. Dhakal, R.; Ntritsos, N.; Cubrinovski, M. Evaluation of liquefaction ejecta potential from case histories and insights from nonlinear dynamic analyses. *J. Geotech. Geoenviron. Eng.* **2026**, *152*, 4025174. [CrossRef]
12. Iai, S.; Matsunaga, Y.; Kameoka, T. Parameter identification for a cyclic mobility model. *Rep. Port. Harb. Res. Inst.* **1990**, *29*, 57–83.
13. Iai, S.; Matsunaga, Y.; Kameoka, T. Strain space plasticity model for cyclic mobility. *Rep. Port. Harb. Res. Inst.* **1990**, *29*, 27–56. [CrossRef] [PubMed]
14. Beaty, M.; Byrne, P.M. An effective stress model for predicting liquefacion behaviour of sand. *Geotech. Earthq. Eng. Soil. Dyn. III ASCE Geotech. Spec. Publ.* **1998**, *1*, 766–777.
15. Zhang, J.-M.; Wang, G. Large post-liquefaction deformation of sand, part I: Physical mechanism, constitutive description and numerical algorithm. *Acta Geotech.* **2012**, *7*, 69–113. [CrossRef]
16. Karamitros, D.K.; Bouckovalas, G.D.; Chaloulos, Y.K. Insight into the Seismic Liquefaction Performance of Shallow Foundations. *J. Geotech. Geoenviron. Eng.* **2013**, *139*, 599–607. [CrossRef]
17. Montoya-Noguera, S.; Lopez-Caballero, F. Effect of coupling excess pore pressure and deformation on nonlinear seismic soil response. *Acta Geotech.* **2016**, *11*, 191–207. [CrossRef]
18. Galavi, V.; Petalas, A.; Brinkgreve, R.B.J. Finite element modelling of seismic liquefaction in soils. *Geotech. Eng.* **2013**, *44*, 55–64.
19. Santisi d'Avila, M.P.; Pham, V.A.; Lenti, L.; Semblat, J.F. Extended Iwan-Iai (3DXii) constitutive model for 1-directional 3-component seismic waves in liquefiable soils: Applicationto the Kushiro site (Japan). *Geophys. J. Int.* **2018**, *215*, 252–266. [CrossRef]
20. Mei, X.; Olson, S.M.; Hashash, Y.M.A. Evaluation of a simplified soil constitutive model considering implied strength and pore-water pressure generation for one-dimensional (1D) seismic site response. *Can. Geotech. J.* **2020**, *57*, 974–991. [CrossRef]
21. Olson, S.M.; Mei, X.; Hashash, Y.M.A. Nonlinear site response analysis with pore-water pressure generation for liquefaction triggering evaluation. *J. Geotech. Geoenviron. Eng.* **2020**, *146*, 4019128. [CrossRef]
22. Tropeano, G.; Chiaradonna, A.; d'Onofrio, A.; Silvestri, F. A Numerical Model for Non-Linear Coupled Analysis on Seismic Response of Liquefiable Soils. *Comput. Geotech.* **2019**, *105*, 211–227. [CrossRef]
23. Chiaradonna, A.; Tropeano, G.; d'Onofrio, A.; Silvestri, F. Development of a simplified model for pore water pressure build-up induced by cyclic loading. *Bull. Earthq. Eng.* **2018**, *16*, 3627–3652. [CrossRef]
24. Terzaghi, K. *Theoretical Soil Mechanics*; John Wiley & Sons, Inc.: Hoboken, NJ, USA, 1943.
25. Chiaradonna, A.; Flora, A.; d'Onofrio, A.; Bilotta, E. A pore water pressure model calibration based on in-situ test results. *Soils Found.* **2020**, *60*, 327–341. [CrossRef]
26. Chiaradonna, A.; Monaco, P.; Tropeano, G. Variability of the seismic response of a liquefiable soil with the fines content as estimated via dilatometer tests. In Proceedings of the 7th International Conference on Geotechnical and Geophysical Site Characterization, Barcelona, Spain, 17–21 June 2024; pp. 1548–1554.
27. Chiaradonna, A.; d'Onofrio, A.; Bilotta, E. Assessment of post-liquefaction consolidation settlement. *Bull. Earthq. Eng.* **2019**, *17*, 5825–5848. [CrossRef]
28. Mele, L.; Chiaradonna, A.; Lirer, S.; Flora, A. A robust empirical model to estimate earthquake-induced excess pore water pressure in saturated and non-saturated soils. *Bull. Earthq. Eng.* **2021**, *19*, 3865–3893. [CrossRef]
29. Chiaradonna, A.; Ntritsos, N.; Cubrinovski, M. CPT-based model calibration for effective stress analysis of layered soil deposits. In *Cone Penetration Testing 2022*; CRC Press: Boca Raton, FL, USA, 2022; pp. 876–882.

30. Chiaradonna, A.; Santisi D'Avila, M.P.; Lenti, L. Seismic response of a 1D soil profile using two modeling approaches in effective stress condition. In Proceedings of the 3rd International Conference on Natural Hazards and Infrastructure, Athens, Greece, 5–7 July 2022.
31. Chiaradonna, A.; Tropeano, G.; d'Onofrio, A.; Silvestri, F. Interpreting the deformation phenomena of a levee damaged during the 2012 Emilia earthquake. *Soil Dyn. Earthq. Eng.* **2019**, *124*, 389–398. [CrossRef]
32. Ausilio, E.; Costanzo, A.; Silvestri, F.; Tropeano, G. Prediction of seismic slope displacements by dynamic stick-slip analyses. *AIP Conf. Proc.* **2008**, *1020*, 475–484. [CrossRef]
33. Tropeano, G.; Ausilio, E.; Costanzo, A. Non-linear coupled approach for the evaluation of seismic slope displacements. In Proceedings of the V International Conference on Earthquake Geotechnical Engineering, Santiago, Chile, 10–13 January 2011.
34. Régnier, J.; Bonilla, L.F.; Bard, P.Y.; Bertrand, E.; Hollender, F.; Kawase, H.; Sicilia, D.; Arduino, P.; Amorosi, A.; Asimaki, D.; et al. International benchmark on numerical simulations for 1D, nonlinear site response (Prenolin): Verification phase based on canonical cases. *Bull. Seismol. Soc. Am.* **2016**, *106*, 2112–2135. [CrossRef]
35. Régnier, J.; Bonilla, L.F.; Bard, P.Y.; Bertrand, E.; Hollender, F.; Kawase, H.; Sicilia, D.; Arduino, P.; Amorosi, A.; Asimaki, D.; et al. PRENOLIN: International Benchmark on 1D Nonlinear Site-Response Analysis—Validation Phase Exercise. *Bull. Seismol. Soc. Am.* **2018**, *108*, 876–900. [CrossRef]
36. Tropeano, G.; Evangelista, L.; Silvestri, F.; d'Onofrio, A. 1D seismic response analysis of soil-building systems including failure shear mechanisms. *Procedia Eng.* **2016**, *158*, 308–313. [CrossRef]
37. Chiaradonna, A.; Tropeano, G.; d'Onofrio, A.; Silvestri, F. A Simplified Method for Pore Pressure Buildup Prediction: From Laboratory Cyclic Tests to the 1D Soil Response Analysis in Effective Stress Conditions. *Procedia Eng.* **2016**, *158*, 302–307. [CrossRef]
38. Kuhlemeyer, R.L.; Lysmer, J. Finite element method accuracy for wave propagation problems. *J. Soil. Mech. Found. Div.* **1973**, *99*, 421–427. [CrossRef]
39. Rayleigh, J.W.S.; Lindsay, R.B. *The Theory of Sound*; Macmillan: New York, NY, USA, 1896.
40. Hashash, Y.M.A.; Park, D. Viscous damping formulation and high frequency motion propagation in non-linear site response analysis. *Soil. Dyn. Earthq. Eng.* **2002**, *22*, 611–624. [CrossRef]
41. Newmark, N.M. A method of computation for structural dynamics. *J. Eng. Mech. Div.* **1959**, *85*, 67–94. [CrossRef]
42. Matasovic, N.; Vucetic, M. Cyclic Characterization of Liquefiable sands. *J. Geotech. Eng.* **1993**, *119*, 1805–1822. [CrossRef]
43. Hashash, Y.M.A.; Musgrove, M.I.; Harmon, J.A.; Ilhan, O.; Xing, G.; Numanoglu, O.; Groholski, D.R.; Phillips, C.A.; Park, D. *DEEPSOIL 7.0, User Manual*; Board Trust Univ Illinois Urbana-Champaign: Urbana, IL, USA, 2020; pp. 1–170.
44. Demir, S. Numerical assessment of the performance of different constitutive models used to predict liquefiable soil behavior. *Int. Adv. Res. Eng. J.* **2021**, *5*, 260–267. [CrossRef]
45. Phillips, C.; Hashash, Y.M.A. Damping formulation for nonlinear 1D site response analyses. *Soil. Dyn. Earthq. Eng.* **2009**, *29*, 1143–1158. [CrossRef]
46. Kramer, S.L. *Geotechnical Earthquake Engineering*; Prentice Hall: Upper Saddle River, NJ, USA, 1996.
47. Kramer, S.L.; Stewart, J.P. *Geotechnical Earthquake Engineering*; CRC Press: Boca Raton, FL, USA, 2024.
48. Chiaradonna, A. Defining the Boundary Conditions for Seismic Response Analysis—A Practical Review of Some Widely-Used Codes. *Geosciences* **2022**, *12*, 83. [CrossRef]
49. Bardet, J.P.; Ichii, K.; Lin, C.H. *EERA a Computer Program for E quivalent-Linear E Arthquake Site Response Analyses of Layered Soil*; University of Southern California: Los Angeles, CA, USA, 2000; p. 40.
50. Kottke, A.R.; Wang, X.; Rathje, E.M. Strata Technical Manual. 2018. Available online: https://github.com/arkottke/strata/releases (accessed on 21 December 2025).
51. Lu, J.; Elgamal, A.-W.M.; Yang, Z. *Cyclic1D: A Computer Program for Seismic Ground Response*; Department of Structural Engineering, University of California: San Diego, CA, USA, 2006.
52. GEO-SLOPE International Ltd. *Dynamic Modeling with QUAKE/W*; GEO-SLOPE International Ltd.: Calgary, AB, Canada, 2014; pp. 1–173.
53. Brinkgreve, R.B.J.; Engin, E.; Swolfs, W.M. PLAXIS 2D Reference Manual 2016. *Plaxis* **2016**, *2016*, 454.
54. Itasca Consulting Group. *Online Manual, FLAC Man*; Itasca Consulting Group: Minneapolis, MN, USA, 2016.
55. Itasca Consulting Group. *FLAC3D—Fast Lagrangian Analysis of Continua in 3 Dimensions, User's Guide*; Itasca Consulting Group: Minneapolis, MN, USA, 2021.
56. OYO Corporation. *Report of Soil Investigation: Sendai District and Onahama District*; Report from the PreNoLin Project; OYO Corporation: Nice, France, 2014.
57. Vucetic, M.; Dobry, R. Effect of soil plasticity on cyclic response. *J. Geotech. Eng.* **1991**, *117*, 89–107. [CrossRef]
58. Cotecchia, V. The reactivation of large flows in the parts of Southern Italy affected by the earthquake of November 23, 1980, with reference to the evolutive mechanism. In Proceedings of the 4th International Symposium on Landslides, Toronto, ON, Canada, 16–21 September 1984; pp. 33–38.

59. Hutchinson, J.N.; Del Prete, M. Landslides at Calitri, southern Apennines, reactivated by the earthquake of 23rd November 1980. *Geol. Appl. Idrogeol.* **1985**, *20*, 1–9.
60. Martino, S.; Mugnozza, G.S. The role of the seismic trigger in the Calitri landslide (Italy): Historical reconstruction and dynamic analysis. *Soil. Dyn. Earthq. Eng.* **2005**, *25*, 933–950. [CrossRef]
61. Palazzo, S. *Progetto Irpinia—Elaborazione dei Risultati Delle Indagini Geotecniche In Sito ed in Laboratorio Eseguite Nelle Postazioni Accelerometriche di Bagnoli Irpino, Calitri, Auletta, Bisaccia, Bovino, Brienza, Rionero in Vulture, Sturno, Benevento e Mercato S*; Sev e Garigliano Ente Naz Energ Elettr (ENEL), Dir delle Costr Rome: Rome, Italy, 1991.
62. Ausilio, E.; Costanzo, A.; Tropeano, G.; Silvestri, F. Evaluation of seismic displacements of a natural slope by simplified methods and dynamic analyses. In *Performance-Based Design in Earthquake Geotechnical Engineering*; Taylor & Francis: London, UK, 2009; pp. 955–962.
63. Stewart, J.P.; Blake, T.M.; Hollingsworth, R.A. Seismic Slope Stability Analyses. In *Guidelines for Analyzing and Mitigating Landslides Hazards in California*; ASCE Los Angeles Section Geotechnical Group: Los Angeles, CA, USA, 2002; Chapter 11; pp. 76–91.
64. Bray, J.D. Simplified seismic slope displacement procedures. In *Earthquake Geotechnical Engineering: 4th International Conference on Earthquake Geotechnical Engineering-Invited Lectures*; Springer: Berlin/Heidelberg, Germany, 2007; pp. 327–353.
65. Itasca, I. *FLAC (Fast Lagrangian Analysis of Continua) Version 7.0*; Itasca Consulting Group: Minneapolis, MN, USA, 2011.
66. Hashash, Y.; Phillips, C.; Groholski, D.R. Recent Advances in Non-Linear Site Response Analysis. Fifth International Conference on Recent Advances in Geotechnical Earthquake Engineering and Soil Dynamics, San Diego, CA, USA, 24–29 May 2010.
67. Matasovic, N.; Hashash, Y.M.A.; National Academies of Sciences, Engineering, and Medicine. *Practices and Procedures for Site-Specific Evaluations of Earthquake Ground Motions*; The National Academies Press: Washington, DC, USA, 2012.
68. Aubry, D.; Modaressi, A. *GEFDYN, Manuel Scientifique*; Ec Cent Paris: Paris, France, 1996.
69. Dafalias, Y.F.; Manzari, M.T. Simple plasticity sand model accounting for fabric change effects. *J. Eng. Mech.* **2004**, *130*, 622–634. [CrossRef]
70. Boulanger, R.W.; Ziotopoulou, K. *PM4Silt (Version 1): A Silt Plasticity Model for Earthquake Engineering Applications*; Center for Geotechnical Modeling, Department of Civil and Environmental Engineering, University of California: Davis, CA, USA, 2018.
71. Matasovic, N. *Seismic Response of Composite Horizontally-Layered Soil Deposits*; University of California: Los Angeles, CA, USA, 1993.
72. Matasovic, N.; Ordonez, G.A. *DMOD 2000: A Computer Program for Nonlinear Seismic Response Analysis of Horizontally Layered Soil Deposits, Earthfill Dams and Solid Waste Landfills*; GeoMotions, LLC.: Lacey, WA, USA, 2011.
73. Moreno-Torres, O.; Hashash, Y.M.A.; Olson, S.M. A simplified coupled soil-pore water pressure generation for use in site response analysis. In Proceedings of the GeoFlorida 2010: Advanced in Analysis, Modeling & Design, West Palm Beach, FL, USA, 20–24 February 2010; pp. 3080–3089.
74. Bažant, Z.P.; Krizek, R.J. Endochronic constitutive law for liquefaction of sand. *J. Eng. Mech. Div.* **1976**, *102*, 225–238. [CrossRef]
75. Valanis, K.C. A theory of viscoplasticity without a yield surface. *Arch. Mech. Stos.* **1971**, *23*, 515–553.
76. Finn, W.D.L.; Bhatia, S.K. Prediction of seismic porewater pressures. *Nucl. Phys. Sect. A* **1981**, *10*, 201–206.
77. Ivšić, T. A model for presentation of seismic pore water pressures. *Soil. Dyn. Earthq. Eng.* **2006**, *26*, 191–199. [CrossRef]
78. Park, D.; Ahn, J. Accumulated stress based model for prediction of residual pore pressure. In Proceedings of the 18th International Conference on Soil Mechanics and Geotechnical Engineering, Paris, France, 2–6 September 2013; pp. 1563–1566.
79. Park, T.; Park, D.; Ahn, J.-K. Pore pressure model based on accumulated stress. *Bull. Earthq. Eng.* **2015**, *13*, 1913–1926. [CrossRef]
80. Seed, H.B. *Representation of Irregular Stress Time Histories by Equivalent Uniform Stress Series in Liquefaction Analyses*; College of Engineering, University of California: Berkeley, CA, USA, 1975.
81. Annaki, M.; Lee, K.L. Equivalent uniform cycle concept for soil dynamics. *J. Geotech. Eng. Div.* **1977**, *103*, 549–564. [CrossRef]
82. Liu, A.H.; Stewart, J.P.; Abrahamson, N.A.; Moriwaki, Y. Equivalent number of uniform stress cycles for soil liquefaction analysis. *J. Geotech. Geoenviron. Eng.* **2001**, *127*, 1017–1026. [CrossRef]
83. Green, R.A.; Terri, G.A. Number of equivalent cycles concept for liquefaction evaluations—Revisited. *J. Geotech. Geoenviron. Eng.* **2005**, *131*, 477–488. [CrossRef]
84. Seed, H.B.; Martin, P.P.; Lysmer, J. Pore-water pressure changes during soil liquefaction. *J. Geotech. Eng. Div.* **1976**, *102*, 323–346. [CrossRef]
85. Boulanger, R.W.; Idriss, I.M. CPT and SPT based liquefaction triggering procedures. *Cent. Geotech. Model.* **2014**, *1*, 134.
86. Mandokhail, S.J.; Park, D.; Yoo, J.-K. Development of normalized liquefaction resistance curve for clean sands. *Bull. Earthq. Eng.* **2017**, *15*, 907–929. [CrossRef]
87. Ntritsos, N.; Cubrinovski, M. A CPT-based effective stress analysis procedure for liquefaction assessment. *Soil. Dyn. Earthq. Eng.* **2020**, *131*, 106063. [CrossRef]
88. Cubrinovski, M.; Ishihara, K. Modelling of sand behaviour based on state concept. *Soils Found.* **1998**, *38*, 115–127. [CrossRef]
89. Cubrinovski, M.; Ishihara, K. State concept and modified elastoplasticity for sand modelling. *Soils Found.* **1998**, *38*, 213–225. [CrossRef]

90. de Cristofaro, M.; Asadi, M.S.; Chiaradonna, A.; Damiano, E.; Netti, N.; Olivares, L.; Orense, R.P. Modeling the Excess Porewater Pressure Buildup in Pyroclastic Soils Subjected to Cyclic Loading. *J. Geotech. Geoenviron. Eng.* **2024**, *150*, 6024007. [CrossRef]
91. Khalil, C.; Régnier, J.; Lopez-caballero, F. LICORNE a benchmark on numerical method for non-linear site response analysis involving pore water pressure. In Proceedings of the 3rd European Conference on Earthquake Engineering & Seismology, Bucharest, Romania, 4–9 September 2022.
92. Chiaradonna, A.; Bilotta, E.; D'Onofrio, A.; Flora, A.; Silvestri, F. A Simplified Procedure for Evaluating Post-Seismic Settlements in Liquefiable Soils. In *Geotechnical Earthquake Engineering and Soil Dynamics V GSP 293 394, Geesd V*; American Society of Civil Engineers: Reston, VA, USA, 2018; pp. 394–403.
93. Chiaradonna, A.; Reder, A. Influence of initial conditions on the liquefaction strength of an earth structure. *Bull. Eng. Geol. Environ.* **2020**, *79*, 687–698. [CrossRef]
94. Chiaradonna, A.; Lirer, S.; Flora, A. A liquefaction potential integral index based on pore pressure build-up. *Eng. Geol.* **2020**, *272*, 105620. [CrossRef]
95. Abdoun, T.; Kokkali, P.; Zeghal, M. Physical Modeling of Soil Liquefaction: Repeatability of Centrifuge Experimentation at RPI. *Geotech. Test. J.* **2018**, *41*, 141–163. [CrossRef]
96. Manzari, M.T.; El Ghoraiby, M.A.; Kutter, B.L.; Zeghal, M. Modeling the cyclic response of sands for liquefaction analysis. In *Earthquake Geotechnical Engineering for Protection and Development of Environment and Constructions*; CRC Press: Boca Raton, FL, USA, 2019; pp. 385–396.
97. Kokkali, P.; Abdoun, T.; Zeghal, M. Physical modeling of soil liquefaction: Overview of LEAP production test 1 at Rensselaer Polytechnic Institute. *Soil. Dyn. Earthq. Eng.* **2017**, *113*, 629–649. [CrossRef]
98. Ghofrani, A.; Arduino, P. Prediction of LEAP centrifuge test results using a pressure-dependent bounding surface constitutive model. *Soil. Dyn. Earthq. Eng.* **2017**, *113*, 758–770. [CrossRef]
99. Adamidis, O.; Madabhushi, G.S.P. Post-liquefaction reconsolidation of sand. *Proc. R. Soc. A Math. Phys. Eng. Sci.* **2016**, *472*, 20150745. [CrossRef]
100. Adamidis, O.; Madabhushi, S.P.G. Experimental investigation of drainage during earthquake-induced liquefaction. *Géotechnique* **2018**, *68*, 655–665. [CrossRef]
101. Ramirez, J.; Barrero, A.R.; Chen, L.; Dashti, S.; Ghofrani, A.; Taiebat, M.; Arduino, P. Site Response in a Layered Liquefiable Deposit: Evaluation of Different Numerical Tools and Methodologies with Centrifuge Experimental Results. *J. Geotech. Geoenviron. Eng.* **2018**, *144*, 04018073. [CrossRef]
102. Ziotopoulou, K. Seismic response of liquefiable sloping ground: Class A and C numerical predictions of centrifuge model responses. *Soil. Dyn. Earthq. Eng.* **2018**, *113*, 744–757. [CrossRef]
103. Cubrinovski, M.; Ishihara, K.; Tanizawa, F. Numerical simulation of the Kobe Port Island liquefaction. In Proceedings of the 11th World Conference on Earthquake Engineering, Acapulco, Mexico, 24–29 June 1996.
104. Zeghal, M.; Elgamal, A.; Parra, E. Analysis of site liquifaction using downhole array seismic records. In Proceedings of the 11th World Conference on Earthquake Engineering, Acapulco, Mexico, 24–29 June 1996.
105. Cubrinovski, M.; Ishihara, K.; Furukawazono, K. Analysis of Two Case Histories on Liquefaction of Reclaimed Deposits. In Proceedings of the 12th World Conference on Earthquake Engineering, Auckland, New Zealand, 30 January–4 February 2000; pp. 1–8.
106. Ishihara, K.; Cubrinovski, M. Characteristics of ground motion in liquefied deposits during earthquakes. *J. Earthq. Eng.* **2005**, *9*, 1–15. [CrossRef]
107. Ziotopoulou, K.; Boulanger, R.W.; Kramer, S.L. Site Response Analysis of Liquefying Sites. *GeoCongress* **2012**, *2012*, 1799–1808.
108. Shibata, T.; Oka, F.; Ozawa, Y. Characteristics of ground deformation due to liquefaction. *Spec. Issue Soils Found.* **1996**, *36*, 65–79. [CrossRef] [PubMed]
109. Das, R.; Sharma, M.L.; Wason, H.R.; Choudhury, D.; Gonzalez, G. A seismic moment magnitude scale. *Bull. Seismol. Soc. Am.* **2019**, *109*, 1542–1555. [CrossRef]
110. Carlton, B. *An Improved Description of the Seismic Response of Sites with High Plasticity Soils, Organic Clays, and Deep Soft Soil Deposits*; University of California: Berkeley, CA, USA, 2014.
111. Paul, S.M.; Chiaradonna, A.; Chiaro, G. Numerical modelling of the dynamic behavior of gravel-rubber mixtures and their efficiency as liquefaction countermeasures. *Jpn. Geotech. Soc. Spec. Publ.* **2024**, *10*, 2414–2419.
112. Dobry, R.; Pierce, W.G.; Dyvik, R.; Thomas, G.E.; Ladd, R.S. *Pore Pressure Model for Cyclic Straining of sand*; Rensselaer Polytechnic Institute: Troy, NY, USA, 1985.
113. Vucetic, M.; Dobry, R. Cyclic triaxial strain-controlled testing of liquefiable sands. *Adv. Triaxial Test. Soil Rock* **1988**, *977*, 475.
114. Chiaradonna, A.; Mohammadi, R.; Monaco, P. Simulation of the Seismic Response of a Man-Made Well-Graded Gravel as Recorded by a Vertical Instrumented Array. *Geo-Congress* **2024**, *2024*, 132–140.

115. Boulanger, R.W.; Ziotopoulou, K. *PM4Sand (Version 3.1): A Sand Plasticity Model for Earthquake Engineering Applications. Rep. No, UCD/CGM-17/01*; Center for Geotechnical Modelling, Department of Civil and Environmental Engineering, University of California: Davis, CA, USA, 2017; 108p.
116. Ziotopoulou, A. Evaluating Model Uncertainty Against Strong Motion Records at Liquefiable Sites. Master's Thesis, University of California, Berkeley, CA, USA, 2010.
117. Arulanandan, K.; Manzari, M.; Zeng, X.; Fagan, M.; Scott, R.F.; Tan, T.S. Significance of the VELACS project to the solution of boundary value problems in geotechnical engineering. In Proceedings of the Third International Conference on Recent Advances in Geotechnical Earthquake Engineering and Soil Dynamics, St. Louis, MI, USA, 1995, 2–7 April 1995.
118. Arulmoli, K.; Muraleetharan, K.K.; Hossain, M.M.; Fruth, L.S. VELACS Laboratory testing program Soil data report. In *The Earth Technology Project n. 90-0562*; The Earth Technology Corporation: Irvine, CA, USA, 1992; Available online: https://www.researchgate.net/publication/269167975_VELACS_Verification_of_Liquefaction_Analyses_by_Centrifuge_Studies_Laboratory_Testing_Program_Soil_Data_Report (accessed on 21 December 2025).